JGR Atmospheres

RESEARCH ARTICLE
10.1029/2024JD042262

# Characterization of the Regional Climate and Large-Scale Atmospheric Circulation in the Caspian Sea Region During the Last Glacial Maximum

**Kim H. Stadelmaier[1], Patrick Ludwig[1], Martin Kehl[2], and Joaquim G. Pinto[1]**

[1]Institute of Meteorology and Climate Research, Troposphere Research (IMKTRO), Karlsruhe Institute of Technology (KIT), Karlsruhe, Germany, [2]Geography Department, Institute for Integrated Natural Sciences, University of Koblenz, Koblenz, Germany

**Key Points:**

- Global climate model data are closer to the proxy data in the Caspian Sea region than in the Mediterranean and Western Europe
- A zonal subtropical jet stream dominates in winter, while a wave-like pattern is formed in summer during the LGM
- LGM circulation weather types are more intense, but in general, the agreement between the models is better on a larger scale perspective

**Supporting Information:**

Supporting Information may be found in the online version of this article.

**Correspondence to:**

K. H. Stadelmaier,
kim.stadelmaier@kit.edu

**Citation:**

Stadelmaier, K. H., Ludwig, P., Kehl, M., & Pinto, J. G. (2025). Characterization of the regional climate and large-scale atmospheric circulation in the Caspian Sea region during the Last Glacial Maximum. *Journal of Geophysical Research: Atmospheres*, *130*, e2024JD042262. https://doi.org/10.1029/2024JD042262

Received 18 AUG 2024
Accepted 4 AUG 2025

**Author Contributions:**

**Conceptualization:** Kim H. Stadelmaier, Patrick Ludwig, Joaquim G. Pinto
**Formal analysis:** Kim H. Stadelmaier
**Funding acquisition:** Patrick Ludwig, Joaquim G. Pinto
**Investigation:** Kim H. Stadelmaier
**Methodology:** Kim H. Stadelmaier, Patrick Ludwig, Joaquim G. Pinto
**Project administration:** Patrick Ludwig, Joaquim G. Pinto
**Resources:** Martin Kehl
**Supervision:** Patrick Ludwig, Joaquim G. Pinto
**Validation:** Kim H. Stadelmaier, Patrick Ludwig, Martin Kehl, Joaquim G. Pinto



**Abstract** The Caspian Sea is the largest inland water body on Earth. Still, this region is often not considered in paleoclimate model analyses. In this study, we examine the climate of the Caspian Sea region during the Last Glacial Maximum (LGM) and its driving large-scale atmospheric circulation using data from two global climate models (AWI-ESM-1-1LR and MPI-ESM1.2-LR) within the PMIP4 framework. We validate the simulation output against proxy data, including information derived from pollen, lake sediments, and loess deposits. Our results demonstrate that the global climate simulations align more closely with proxy data within the Caspian Sea region (mostly within one standard deviation) than the Mediterranean and Western Europe and can thus be further exploited. The subtropical jet stream is dominant in winter exhibiting higher wind speeds than in summer, where the jet stream undergoes a transition from a zonal structure under preindustrial conditions to a wave-like pattern during the LGM. Furthermore, there is an increase in extratropical cyclone activity during the LGM. The analysis of the near-surface circulation reveals the dominance of an anticyclonic flow in summer, which becomes even more frequent during the LGM (increase by up to 20%). The general characteristics of the rotational circulation weather types change toward an intensification during the LGM. Overall, the models demonstrate greater agreement at larger scales. However, to enable a more direct comparison with local proxy data, especially in the topographically complex region along the southern coast of the Caspian Sea, we suggest a follow-up study employing high-resolution climate simulations.

**Plain Language Summary** The Last Glacial Maximum (LGM) was a cold and dry period around 20,000 years ago. The climate was very different from today, and ice sheets covered much of the Northern Hemisphere. The focus of this study is the region around the Caspian Sea. The Caspian Sea is the largest lake in the world and is located on the border between Asia and Europe. Using data of two state-of-the-art global climate models with 200 km horizontal resolution, we first analyze the climate of the Caspian Sea region during the LGM and compare the model output with geological evidence (e.g., pollen data) for temperature and precipitation changes. Furthermore, we study the atmospheric dynamics that drive the regional climate. This includes the upper-level atmospheric jet stream, storm activity, and near-surface atmospheric circulation weather types. The Caspian Sea region is better represented in the models than Western Europe and the Mediterranean region in terms of temperature and precipitation changes. The two climate models show greater agreement at larger scales than on local scales of the geological evidence. Thus, we recommend employing high-resolution climate model simulations to bridge the gap between the coarse global simulations and to enable a more precise comparison with proxy data.

## 1. Introduction

The Caspian Sea is the largest inland water body on Earth, with a volume of 78,000 km$^3$ and a surface area of 392,000 km$^2$. It extends 320 km on average in east-west, and 1030 km in total in north-south direction (Haghani & Leroy, 2020; Kosarev, 2005). The Caspian Sea comprises several climate zones, ranging from subtropical, humid conditions in the south, to a warm and arid continental climate in the north and northeast (Nandini-Weiss et al., 2020). The surrounding vegetation is equally diverse: The north and northeast is characterized by a salt desert and steppe, while the Hyrcanian forest to the south of the Caspian Sea forms a narrow, biodiverse refuge for past European species (Haghani & Leroy, 2020; Kosarev, 2005; Molavi-Arabshahi et al., 2016). Sured by high mountain ranges with the Caucasus Mountains to the west, and the Elburz mountain range to the south, the

**Visualization:** Kim H. Stadelmaier
**Writing – original draft:** Kim H. Stadelmaier
**Writing – review & editing:** Kim H. Stadelmaier, Patrick Ludwig, Martin Kehl, Joaquim G. Pinto

Caspian Sea region is characterized by a complex topography. Particularly the southern coast of the Caspian Sea shows a sharp slope from the water level at −27 m above sea level (a.s.l.), to the highest peaks of the Elburz mountain range reaching 5000 m a.s.l., at a distance of about 70 km.

Today, the main large-scale atmospheric circulation features in the Caspian Sea region are the midlatitude westerlies, such as the polar and subtropical jets, and the Siberian and the subtropical high pressure systems (Akçar & Schlüchter, 2005; Nandini-Weiss et al., 2020; Wegwerth et al., 2021; Wigley & Farmer, 1982). During wintertime, cold Arctic air masses as well as dry and cold continental air masses from the Siberian anticyclone are often transported into the region across its north and east borders. Furthermore, temperate humid air masses from the North Atlantic and subtropical warm air masses from the Mediterranean Sea, Black Sea, and Iranian plateau influence the regional climate (Kosarev, 2005; Kosarev et al., 2014; Molavi-Arabshahi et al., 2016; Wegwerth et al., 2021). The northern Caspian Sea is more often exposed to extratropical cyclonic activity, where northerly winds dominate according to Kosarev et al. (2014). For the southern Caspian Sea, 75% of the extratropical cyclones occur in winter and are warm-cored midlatitudinal systems from the Mediterranean and Black Seas, while in summer, the storm track is shifted northward due to the presence of the subtropical high pressure systems (Molanejad et al., 2015).

These general atmospheric features have changed during the Last Glacial Maximum (LGM), a period that is defined as the most recent interval of maximum global ice volume (Clark et al., 2009; Mix et al., 2001). During this period, which corresponds to around 26–19 thousand years before present (ka BP), large ice sheets covered the Northern Hemisphere and the global sea level was 130 m lower during the coldest phase of the LGM and thus at a historic minimum (Lambeck et al., 2014). Atmospheric greenhouse gas concentrations were less than half of today's, favoring C4 plants over C3 plants and leading to a less productive ecosystem with more open vegetation (Bartlein et al., 2011; Monnin et al., 2001; Prentice & Harrison, 2009). These boundary conditions led to a globally colder and drier climate with an altered large-scale atmospheric circulation (e.g., Annan & Hargreaves, 2013; Bartlein et al., 2011). The changes of the topography by the high northern hemispheric ice sheets induced a large-scale atmospheric wave in the midlatitudes, leading to more zonally orientated jet stream over the North Atlantic. Due to an enhanced temperature gradient between the Arctic and the tropics, the midlatitude jet stream was intensified and shifted southward (Justino & Peltier, 2005; Li & Battisti, 2008; Löfverström et al., 2014; Merz et al., 2015; Pausata et al., 2011) with the associated storm tracks evolving accordingly (Klige & Myagkov, 1992; Löfverström et al., 2014; Ludwig et al., 2016; Pfahl et al., 2015; Pinto & Ludwig, 2020; Raible et al., 2021). During the LGM, extreme cyclones had different characteristics compared to present day. They carried less moisture but exhibited enhanced wind speeds, which had the potential to trigger strong dust events. The generally drier and windier conditions during the LGM led to the formation of large loess deposits throughout Europe and Asia (Pfahl et al., 2015; Pinto & Ludwig, 2020; Schaffernicht et al., 2020; Sima et al., 2009).

Loess deposits from the southern Caspian basin indicate that this region was also considerably drier than the comparatively humid periods of the last or present interglacials or of interstadials of the early Last Glacial. The drier climate of the LGM is indicated by high dust deposition rates similar to earlier phases of the Last Pleniglacial (MIS 4 to MIS 2) in the area (e.g., Frechen et al., 2009; Ghafarpour et al., 2024; Kehl et al., 2021; Lauer, Frechen, et al., 2017; Lauer, Vlaminck, et al., 2017; Vlaminck et al., 2018). However, there are reports on the presence of a paleosol at a depth of ca. 3 to 4 m below land surface sandwiched by layers of weakly weathered loess. The paleosol is an indicator of slightly more humid climate and lower dust accumulation rates, whereas loess layers indicate dry climate and higher dust accumulation rates. The paleosol, however, is much less well developed than the modern soil and can thus only represent an interstadial soil. Two papers have provided luminescence age estimates for the accumulation of loess sandwiching this paleosol. According to Maleki et al. (2023), loess below this paleosol accumulated after ca. 24.3 ± 1.6 and before 16.6 ± 1.1 ka BP, whereas Lauer, Frechen, et al. (2017) yielded ages of 26.0 ± 1.7 ka BP and 25.1 ± 1.8 ka BP. Given the error margins, both paleosols may have formed at the same time, but only the one studied by Maleki et al. (2023) may fall in the LGM. It should be noted that both loess sections studied are located in the area of Gorgan, at just 3.5 km distance as the crow flies. Ghafarpour et al. (2024) described a weakly developed paleosol at about 3.5 m depth below the land surface dated to have formed between 16.5 ± 1.5 and 13.0 ± 0.9 ka BP. This paleosol was obviously formed after the LGM, possibly during an interstadial of the late glacial. In alluvial sediments of the Caspian lowlands, another paleosol developed after ca. 28 ka cal PB and before 12 ka cal BP (Antoine et al., 2006) and testifies to increased moisture supply. The precise age of the mentioned paleosols is still not well defined. However, they are weakly developed and apparently formed during a shorter period of time; hence, they are not an indicator of a much more humid

climate, similar as other weakly developed paleosols intercalated in Last Glacial loess of the area. Overall, the climate was dry and dust accumulation rates high. Climate model studies within the framework of the Palaeoclimate Modelling Intercomparison Project (PMIP) Phase 3 reveal a weaker hydrological cycle during the LGM over arid central Asia (Xu et al., 2020), but an increase in the annual runoff of the Volga River mainly accounted by snow melt (Kalugin & Morozova, 2023). The slightly increased humidity suggested by the abovementioned paleosols may indicate a transgression state of the Caspian Sea during the LGM (Kehl et al., 2021; Vlaminck et al., 2018), although dating uncertainties remain significant.

The water level of the Caspian Sea varied substantially during the Late Pleistocene. The definition and separation of different regression and transgression states is relatively well understood (e.g., Dolukhanov et al., 2010; Yanina et al., 2021). On the other hand, there is no consensus about the chronology and absolute dates of these phases and thus also for the state of the Caspian Sea during the LGM (e.g., Krijgsman et al., 2019; Tudryn et al., 2022, for comprehensive review papers). The lowest water level during the Late Pleistocene occurred during the Atelian regression with −100 m a.s.l. Conversely, the Early Khvalynian highstand at +50 m a.s.l. resulted in a much larger Caspian Sea than today.

While the climate and atmospheric dynamics during the LGM are relatively well studied for East Asia with focus on the East Asian winter monsoon, Europe, and North America (e.g., Amaya et al., 2022; Izumi et al., 2023; Jouvet et al., 2023; Lei et al., 2021; Lu et al., 2025; Oster et al., 2015; Peng et al., 2024; Schaffernicht et al., 2020), the Caspian Sea region is underrepresented in modeling studies as for example, within the framework of the Palaeoclimate Modelling Intercomparison Project (PMIP). With the unique topography of the Caspian Sea region, results are not easily transferrable from other regions. Therefore, the main goal of this study is to assess the climate of the Caspian Sea region during the LGM and its driving large-scale atmospheric circulation using state-of-the-art global climate models within the framework of PMIP Phase 4 (Kageyama et al., 2017). Specifically, (a) we assess how well the LGM climate of the Caspian Sea region is represented in global climate models within the PMIP4 framework compared to other regions in Europe and the Mediterranean based on proxy evidence and (b) evaluate changes in the large-scale atmospheric features that drive the climate in the Caspian Sea region during the LGM compared to the preindustrial (PI) period. Ultimately, (c) we assess the regional differences of the near-surface atmospheric circulation and associated precipitation patterns in the Caspian Sea region during the LGM.

We introduce the proxy data and global climate models used for this study, and the methods applied to exploit the aforementioned research questions in Section 2. Results are presented in Section 3, and are subsequently discussed and summarized in Section 4.

## 2. Data and Methods

In this study, we analyze the climate and the large-scale atmospheric circulation of the Caspian Sea region using global climate model (GCM) simulations conducted within the PMIP4 framework (Kageyama et al., 2017). Time-slice experiments of the LGM and the PI from two GCMs are considered, namely from the models MPI-ESM1.2-LR (MPI; Mauritsen et al., 2019) and AWI-ESM-1-1-LR (AWI; Lohmann et al., 2020; Sidorenko et al., 2015). The horizontal resolution of both global models is 1.85°, corresponding to approximately 200 km. The simulations follow the PMIP4 protocol, which specifies the boundary conditions for the LGM and PI, for example, atmospheric greenhouse gas concentrations, implemented ice sheets, and solar insolation (Kageyama et al., 2017; Eyring et al., 2016, respectively). The selection criterion to choose the models used in this work is that those models are the only ones that provide 6-hourly output data, which is a requirement for the executed analysis methods. Furthermore, we ensured that the models are well within the PMIP4 ensemble range. This is the case for the mean annual air temperature for both the global average as well as in the northern extratropics (30°N–90°N), albeit with less cooling during the LGM than the PMIP4 ensemble mean (Kageyama et al., 2021). Mean annual air temperature anomaly features such as land-sea contrast and polar amplification are captured, with the MPI simulations being among the closest to proxy reconstructions, and the AWI simulations are still closer to reconstruction than many other models (Kageyama et al., 2021, see Figures 10 and 11 therein). Regarding precipitation changes during the LGM, both AWI and MPI model simulations have less pronounced reduction of precipitation than the ensemble mean on global average and on average over the northern extratropics. However, the PMIP4 models do not agree on the direction of precipitation changes in the Caspian Sea region (Kageyama et al., 2021, see Figure 6 therein). For each experiment considered in this study, we analyze 30 consecutive years of the 100–1,000 years lasting simulations with relatively stable conditions in three variables of our interest

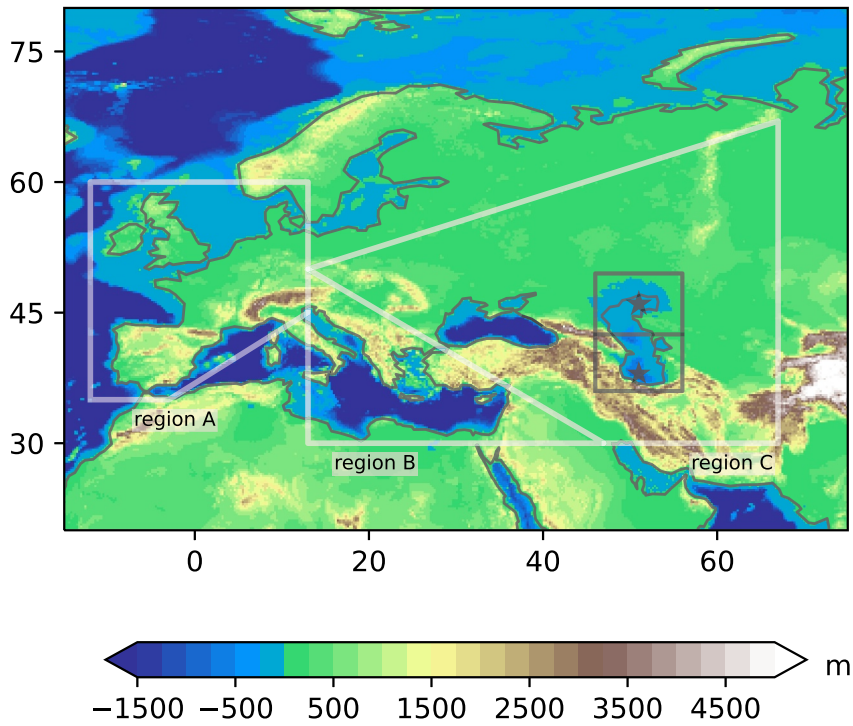


**Figure 1.** Topography of the region of interest based on NOAA (2022). White polygons indicate regions for which a model-proxy data comparison is computed. The regions are representative for Western Europe (region A), Mediterranean (region B), and the Pontocaspian region (region C). Black stars show center points for the circulation weather type (CWT) calculations: the northern Caspian Sea (NCS) at 46°N; 51°E and the southern Caspian Sea (SCS) at 38°N; 51°E. Black boxes indicate regions for which the associated precipitation per CWT is calculated.

representing the climate and atmospheric dynamics, that is, 2 m air temperature, total precipitation, and zonal wind speed in 200 hPa and decided for a 30-year analysis window as recommended by the World Meteorological Organization (WMO) as a standard period of reference (WMO, 2017). The exact criteria and selected time slices are described in Supporting Information S1.

To assess the ability of the PMIP4 GCMs in representing the LGM climate, we compare the deviations of 2 m air temperature and total precipitation for PI conditions to proxy data from Bartlein et al. (2011). These variables can be derived from various types of proxy data with relative certainty and are thus well suited for comparison with model data. The proxy data from Bartlein et al. (2011) are only available for specific locations on a 2° × 2° grid (Bartlein et al., 2011, see Figure S2 in Supporting Information S1). We calculated the mean and standard deviation of the proxy data for three different areas with similar amounts of data points that are representative for the regions: Western Europe (region A), Mediterranean (region B), and the Pontocaspian region (region C); see white polygons in Figure 1. This aggregation of data points may mask local variability but is necessary to enhance the robustness of the comparison between local proxy data and coarse resolution global model data. The proxy data are then quantitatively compared to the simulated regional average values, which are computed after an interpolation of the data on the same 2° × 2° grid. A point-to-point comparison can be found in Supporting Information S1, Tables S2–S5.

The large-scale atmospheric circulation over the region is now examined focusing on the jet stream location and intensity (zonal wind speed in 200 hPa) and the storm track activity. These are typical variables to assess the synoptic activity and variability. The storm track activity is quantified by the standard deviation of the 2.5–6 days band-pass filtered 6-hourly geopotential height at 850 hPa (Hoskins & Valdes, 1990), where 2.5–6 days correspond to the so-called synoptic scale, whose variability is primarily due to the passage of low pressure centers. The method has been used for different types of gridded atmospheric data, typically mean sea level pressure data (Ulbrich et al., 2008). However, due to the high topography in the region of interest, the storm track diagnostic is

derived from a higher altitude, namely 850 hPa, roughly corresponding to 1500 m a.s.l. to avoid topographic noise.

To assess the regional atmospheric circulation, we applied the circulation weather type (CWT) approach based on Jones et al. (1993). With this approach, the daily atmospheric circulation is classified into eight directional CWTs: northeast (NE), east (E), southeast (SE), south (S), southwest (SW), west (W), northwest (NW), and north (N), and two rotational CWTs: cyclonic (C) and anticyclonic (A). For each day, the directional flow F and the vorticity Z at a given central point is calculated considering 16 surrounding grid points on a regular 2.5° × 2.5° grid. In the original method, the calculation is based on mean sea level pressure data. In this study, however, daily geopotential height data at 850 hPa are considered, following Reyers et al. (2013) and to account for the high topography in the region of interest. Two different central points are chosen in this study to analyze the circulation differences between the northern (NCS; 46°N; 51°E) and southern (SCS; 38°N; 51°E) parts of the Caspian Sea basin, where the northern part is embedded in lowland areas with dry continental climate and the southern part is surrounded by high topography. The two central points are furthermore motivated based on the jet stream position. The northern point is located within the area of influence of the westerly wind zone of the jet, whereas the southern point is in the periphery of the jet. The frequency of occurrence for each CWT and the associated amount of precipitation are calculated for both regions shown in Figure 1 individually as stars: 46°E–56°E and 36°N–42.5°N for SCS and 42.5°N–49.5°N for NCS.

## 3. Results

### 3.1. Simulated Climate in the Caspian Sea Region Compared to Proxy Data

In this section, we present the simulated climate of the PI and LGM in terms of annual mean 2 m air temperature and total precipitation in Europe and the Caspian Sea region (see Figure 2) and an evaluation of the simulated changes between LGM and PI against available proxy data.

The annual mean 2 m air temperature distributions are similar for the AWI and MPI models under PI conditions, with the MPI simulation being slightly colder (Figures 2a and 2c). The lowest temperatures are located over the Himalaya and in the northeast of the depicted maps. The temperatures increase from north to south and slightly from east to west. The cooling under LGM conditions is significant at a 99% confidence level across most of the considered region. The largest temperature drops, by 28°C for both models, occur over the Fennoscandian ice sheet, with decreasing magnitude toward the south (Figures 2b and 2d). Over water bodies such as the Mediterranean Sea and the (deeper southern) Caspian Sea, the cooling is also less distinct. The differences between LGM and PI simulations are less homogeneous in the AWI simulations, and the cooling is less pronounced than in the MPI simulations.

Under PI conditions, a band with high daily precipitation values extends from the North Atlantic to Siberia with decreasing intensity eastward in both GCMs, as expected from a diminishing influence of Atlantic air masses (Figures 2e and 2g). The MPI simulations show more precipitation than the AWI simulation. This relation is reversed when it comes to LGM minus PI differences. Both simulations show a decrease of annual mean precipitation under LGM conditions over the ice sheet and to its east, and an increase over the Iberian Peninsula and the Mediterranean region (Figures 2f and 2h). This increase extends further east along the northern coast of the Black Sea and the Caspian Sea only in the AWI simulations. The increase in precipitation over the Iberian Peninsula is a well-known issue in global climate model simulations of the LGM and can mainly be attributed to higher sea surface temperatures (SSTs), the thereby increased atmospheric moisture and the implemented vegetation distribution (Ludwig et al., 2017). The discrepancy between simulated and proxy data is also evident in our analysis (see last column of Table 1). Although proxy data suggest a strong decrease in annual mean precipitation, both models show an increase over Western Europe (region A) and the Mediterranean region (region B). However, the decrease of precipitation in the Pontocaspian region during LGM is captured better by the MPI simulations than in the AWI simulations (Table 1). The largest precipitation decrease is located at the eastern coast of the Black Sea according to the data from Bartlein et al. (2011, see Figure S2c in Supporting Information S1), while the northern Pontocaspian region shows only a moderate decrease. Southeast of the Caspian Sea, no data point is available. The MPI model agrees in the overall reduction except for the western Black Sea region, although the largest differences arise east of the FIS. The AWI model, with the increase of precipitation north of the Caspian Sea, agrees only with the proxy data in regions of simulated precipitation reduction (see Figure 2 and Figure S2c in Supporting Information S1).

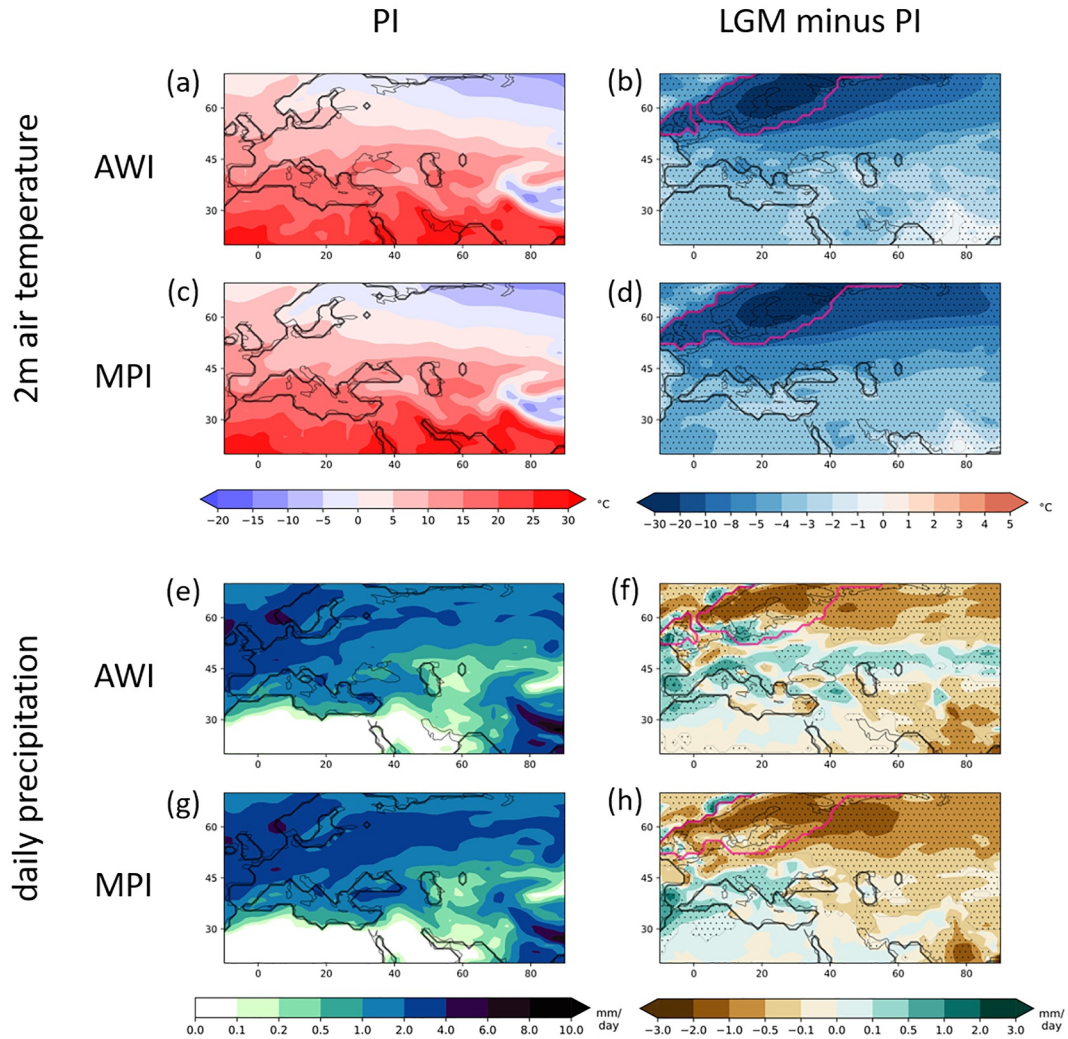


**Figure 2.** Distributions of annual means of 2 m air temperature (a–d) and total precipitation (e–h) as simulated by the AWI and the MPI models. Absolute fields of the PI simulations are displayed in the first column; the second column represents LGM minus PI differences. Black lines denote the respective implemented coastlines (left column: PI and right column: LGM), and pink lines mark the ice sheet extent during the LGM. Dotted areas indicate a significant change between LGM and PI simulations based on a two sided bootstrap *t* test at a 99% confidence interval.

Both GCMs capture the temperature differences more accurately than precipitation levels in all three regions. The amplitude of the changes vary, and the MPI simulations are generally slightly closer to the proxy data. Although the temperature difference of the coldest month is well represented in the Pontocaspian region by the models compared to proxy evidence, the temperature difference of the warmest month is not accurately captured. This, however, is within the error estimates for the other two regions.

Overall, the global simulations reasonably represent the expected differences between LGM and PI climates and can thus be used for further analysis.

### 3.2. Large-Scale Dynamics Driving the Climate of the Caspian Sea Region

In this section, we assess the large-scale atmospheric dynamics influencing the climate of the Caspian Sea region. Therefore, the long-term mean zonal wind speed in 200 hPa over the winter months (December–January–February; DJF) and the summer months (June–July–August; JJA) are shown in Figure 3 to derive the polar and subtropical jet characteristics. The associated mean winter and summer storm tracks are displayed in Figure 4.

**Table 1**
*Model-Proxy Comparison for LGM Minus PI Values of Annual Mean Temperature ($T_{ann}$), Temperature of the Coldest Month ($T_{cold}$), and Temperature of the Warmest Month ($T_{warm}$; All Temperatures in °C) and Annual Mean Precipitation (Precip, in mm/Year) for the Three Regions are Marked in Figure 1*

| | | $T_{ann}$ [°C] | $T_{cold}$ [°C] | $T_{warm}$ [°C] | Precip [mm/year] |
|---|---|---|---|---|---|
| Region A | Proxy | **−8.5 ± 2.0** | **−16.7 ± 3.1** | **−6.2 ± 1.3** | **−394.5 ± 101.7** |
| | # Data points | 7 | 7 | 7 | 7 |
| | AWI | −3.8 | −2.2 | −6.7 | 122.4 |
| | MPI | −4.6 | −4.6 | −5.4 | 2.7 |
| Region B | Proxy | **−5.8 ± 2.0** | **−14.6 ± 3.3** | **−5.0 ± 1.7** | **−231.9 ± 100.5** |
| | # Data points | 9 | 10 | 10 | 10 |
| | AWI | −3.8 | −2.6 | −5.2 | 7 |
| | MPI | −3.9 | −3.8 | −4.5 | 59.1 |
| Region C | Proxy | **−9.0 ± 1.5** | **−14.0 ± 3.2** | **−5.8 ± 0.9** | **−183.2 ± 77.7** |
| | # Data points | 13 | 13 | 13 | 11 |
| | AWI | −6.5 | −7.7 | −3.7 | −47.8 |
| | MPI | −7.5 | −11.3 | −3.2 | −156.3 |

*Note*. Proxy data are given by Bartlein et al. (2011) with LGM minus PI values and standard error of reconstruction. Dark green shading: simulated change within standard error estimates. Midgreen: simulated change within 1.5 times standard error of estimates. Light green: simulated change within 2 times standard error of estimates.

The overall structure and strength of the zonal wind speed in 200 hPa is similar in the AWI and MPI simulations under PI conditions (Figure 3). The subtropical jet dominates in winter, with strong wind speeds over the Mediterranean Sea and south of the Black Sea and southern Caspian Sea. In the MPI simulation, the jet extents slightly northward. During the LGM, the subtropical jet is by up to 8 m/s weaker, but wind speeds on its north flank are higher (Figure 3d). The AWI simulations reveal a stronger jet that penetrates further into the continent, leading to stronger winds over the Black Sea and the Caspian Sea (Figure 3b). The differences between LGM and PI are zonally structured and significant at the 99% confidence level. Differences in the MPI simulations are weaker and not as significant. Coherent structures are the rather zonal patterns, with higher background wind speeds in northern Eurasia and north of the Caspian Sea and the weaker subtropical jet. In summer, both models reveal a zonal jet stream that is weaker than in winter, with a maximum over the northern Caspian Sea and eastward in the PI (Figures 3e and 3g). The differences between LGM and PI are similar, and show a quadrupole structure with two regions of up to 8 m/s weaker wind speeds, one over the Fennoscandian ice sheet (FIS) and one over the Caspian Sea (Figures 3f and 3h). The Mediterranean Sea and the region north of the Caspian Sea/east of FIS are connected via high wind speeds. The summer jet stream forms a wave-like pattern, unlike the zonal jet stream in the PI.

In agreement with the jet stream, the storm track activity is highest in winter for both models and periods (Figure 4). Storm tracks are restricted to northern Europe and Eurasia in the PI in both models (Figures 4a and 4c). The region of high storm track activity in the PI is affected by the FIS during the LGM, which blocks the storms and deflects them southward. This leads to an enhanced storm track activity over southern Europe and the Mediterranean region during the LGM (Figures 4b and 4d). The MPI simulations show weaker and less significant differences, but here also, the overall storm track activity intensified and is shifted to the south. During summer, the storm track activity is restricted to northern parts of the region with the highest activity over Scandinavia (Figures 4e and 4g). Over southern Europe and the Pontocaspian region, the storm track activity is very low for the PI. During the LGM, the overall storm track activity is enhanced, particularly in a region extending from central Europe to the northern Pontocaspian region (Figures 4f and 4h). South of the Caspian Sea, there is almost no increase during the LGM, which is in line with the shifted jet stream position.

### 3.3. Atmospheric Circulation of the Caspian Sea Region

The dominant regional atmospheric flow regimes are assessed by the circulation weather type approach after Jones et al. (1993) for two locations in the Caspian Sea (north and south; see Figure 1). We analyze the CWTs in

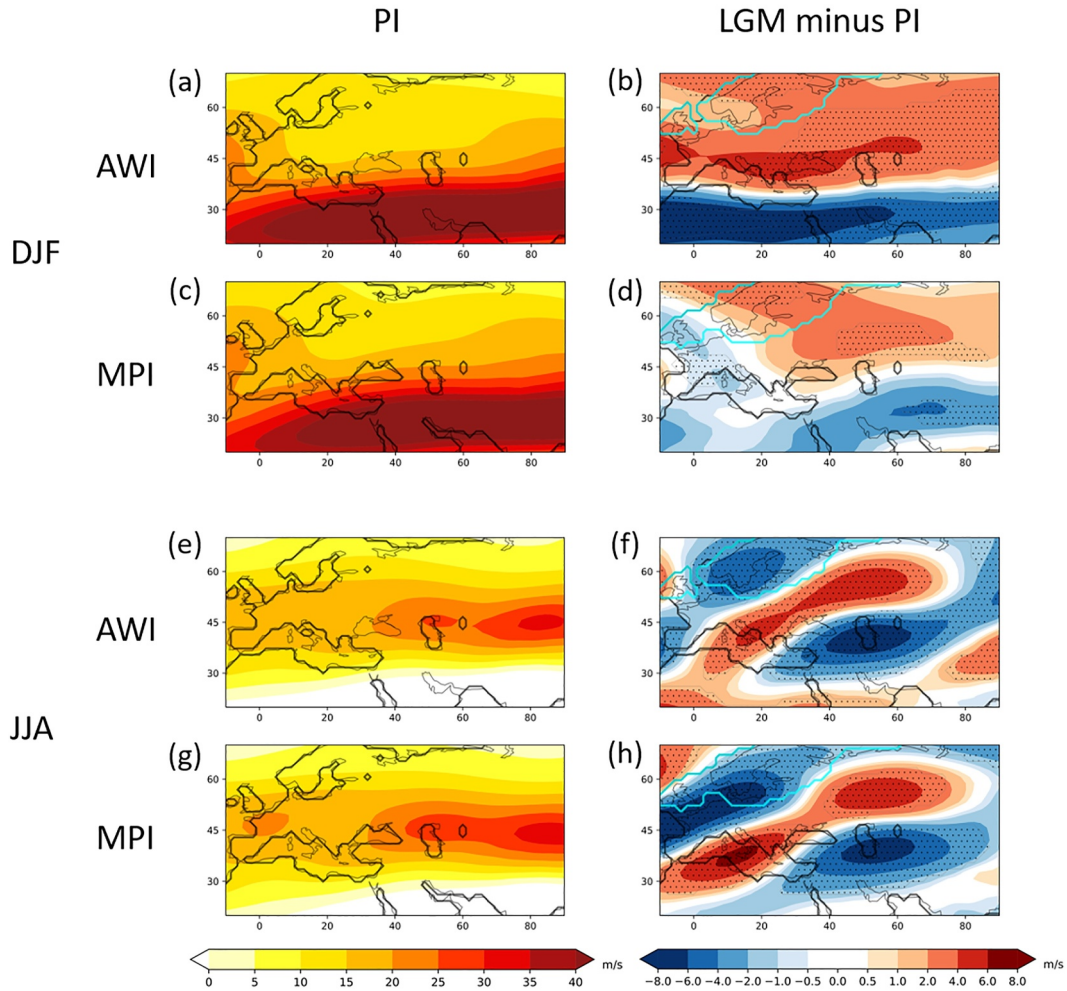


**Figure 3.** Distributions of 200 hPa wind speed in winter (a–d) and summer (e–h) as simulated by the AWI and the MPI models. Absolute fields of the PI simulations are displayed in the first column, the second column represents LGM minus PI differences. Black lines denote the respective implemented coastlines (left column: PI; right column: LGM), and cyan lines mark the ice sheet extent during the LGM. Dotted areas indicate a significant change between LGM and PI simulations based on a two-sided bootstrap *t* test at a 99% confidence interval.

terms of their occurrence frequency, their associated precipitation patterns, and the characteristics of two exemplary CWTs (cyclonic and anticyclonic) in the southern Caspian Sea region.

Strong westerlies approach Europe from the North Atlantic and along the Mediterranean Sea in winter in the PI (see Figures 5a and 5d) in both GCMs. The winds are overall stronger in the MPI simulation, and the wind regime over the Caspian Sea is divided into prevailing westerlies in the northern part and south-westerlies in the southern part. The stronger winds are not further enhanced in the LGM in the MPI simulation, despite some regions south of the Mediterranean Sea, and slightly but significantly south to the Caspian Sea (Figures 5e and 5f). However, this is not the case in the AWI LGM simulation. Here, a strong increase is simulated in a broad band from the North Atlantic to the Caspian Sea and further eastward (Figures 5b and 5c). Both models show a decrease in wind over Scandinavia due to the altered wind directions over the Fennoscandian ice sheet. Both simulations indicate that summer winds are less strong and less enhanced during the LGM (Figures 5i and 5l). East of the Caspian Sea, northerly winds divide from the westerly wind band, which are enhanced during the LGM.

The CWT occurrence frequencies for the PI and LGM are displayed in Figure 6 for both locations and models. For PI, the winter frequency distributions are similar in both regions and models, with westerly winds dominating (Figure 6, left column). Together with the south-westerly and north-westerly CWTs, they account for more than 50% of all analyzed winter days in the AWI simulation and for even two thirds in the MPI simulation over the

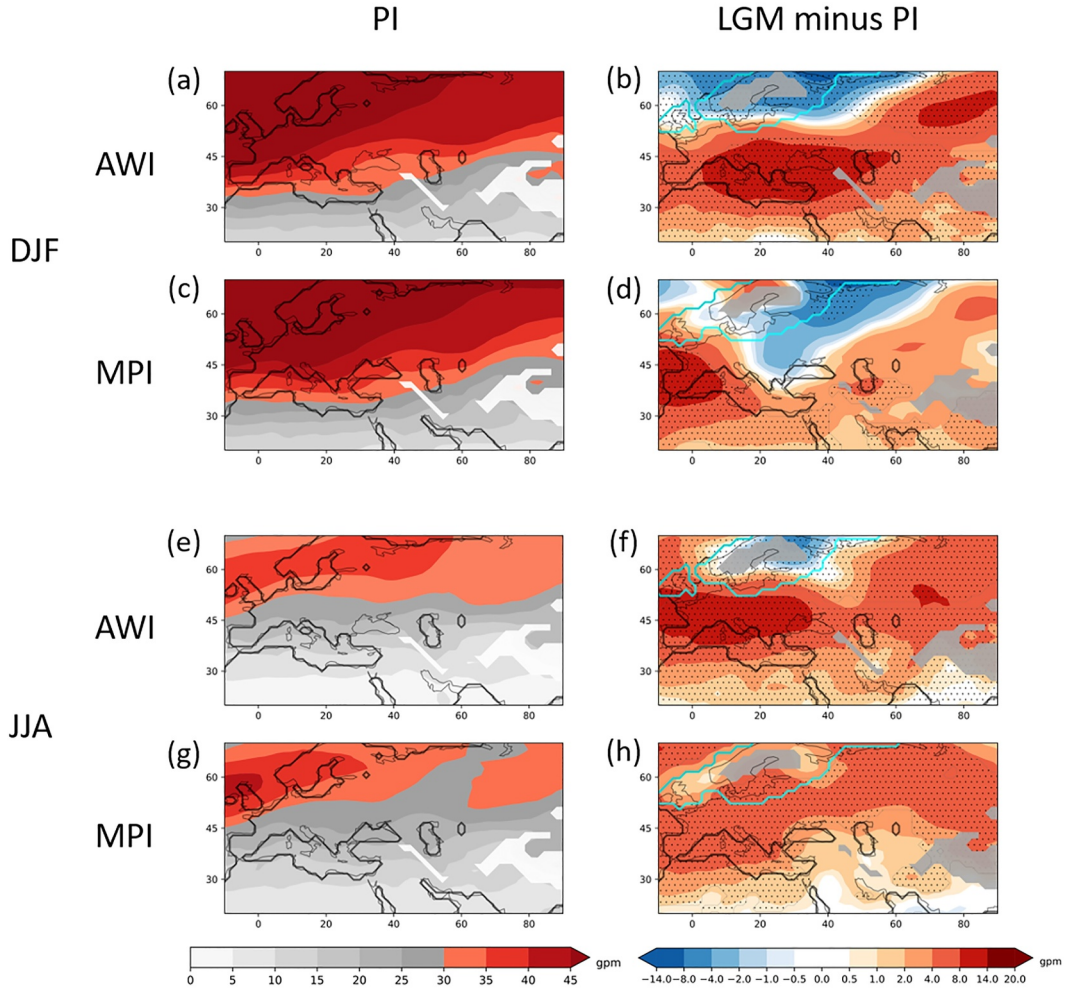


**Figure 4.** Distributions of storm track activity based on 850 hPa geopotential in winter (a–d) and summer (e–h) as simulated by the AWI and the MPI models. Absolute fields of the PI simulations are displayed in the first column, and the second column represents LGM minus PI differences. Black lines denote the respective implemented coastlines (left column PI; right column: LGM), and cyan lines mark the ice sheet extent during the LGM. Areas with topography higher than 1500 m a.s.l. are masked in white (left column) and gray (right column). Dotted areas indicate a significant change between LGM and PI simulations based on a two-sided bootstrap *t* test at a 99% confidence interval.

southern Caspian Sea and slightly less over the northern Caspian Sea. While the rotational CWTs also play a role in winter, easterly winds are very rare. During summer, the prevailing wind direction over the southern Caspian Sea is reversed, resulting in predominately easterly and anticyclonic circulation types (Figure 6g). Anticyclonic circulation dominates over the northern Caspian Sea, but westerly winds still occur relatively frequently (Figure 6e). In contrast, cyclonic circulation is rare during summer at both locations. Regarding the differences between the LGM and PI, the models agree only partly. In winter, the low frequencies of easterly circulation types are further reduced, while westerly CWTs occur more often (Figures 6b and 6d). Changes of cyclonic and anticyclonic CWTs partly contradict between the two GCMs. Summer changes over the northern Caspian Sea show less north and north-westerly flow (Figure 6f). As in the southern Caspian Sea in summer (Figure 6h), easterly circulation types occur less often and, for MPI, the anticyclonic CWT occurrence frequency is enhanced. In the AWI simulations, this enhancement leads to an occurrence frequency of 48% for the anticyclonic CWT alone.

The relative contributions to annual precipitation by each CWT are shown in Figure 7. The Caspian Sea region experiences higher precipitation during winter, with the westerly and cyclonic CWTs being the main contributors (Figures 7a and 7c), although the occurrence frequency of the cyclonic CWT is low (Figures 6a and 6c). In the southern Caspian Sea, also the northerly CWTs are linked to precipitation that probably forms as air flows over

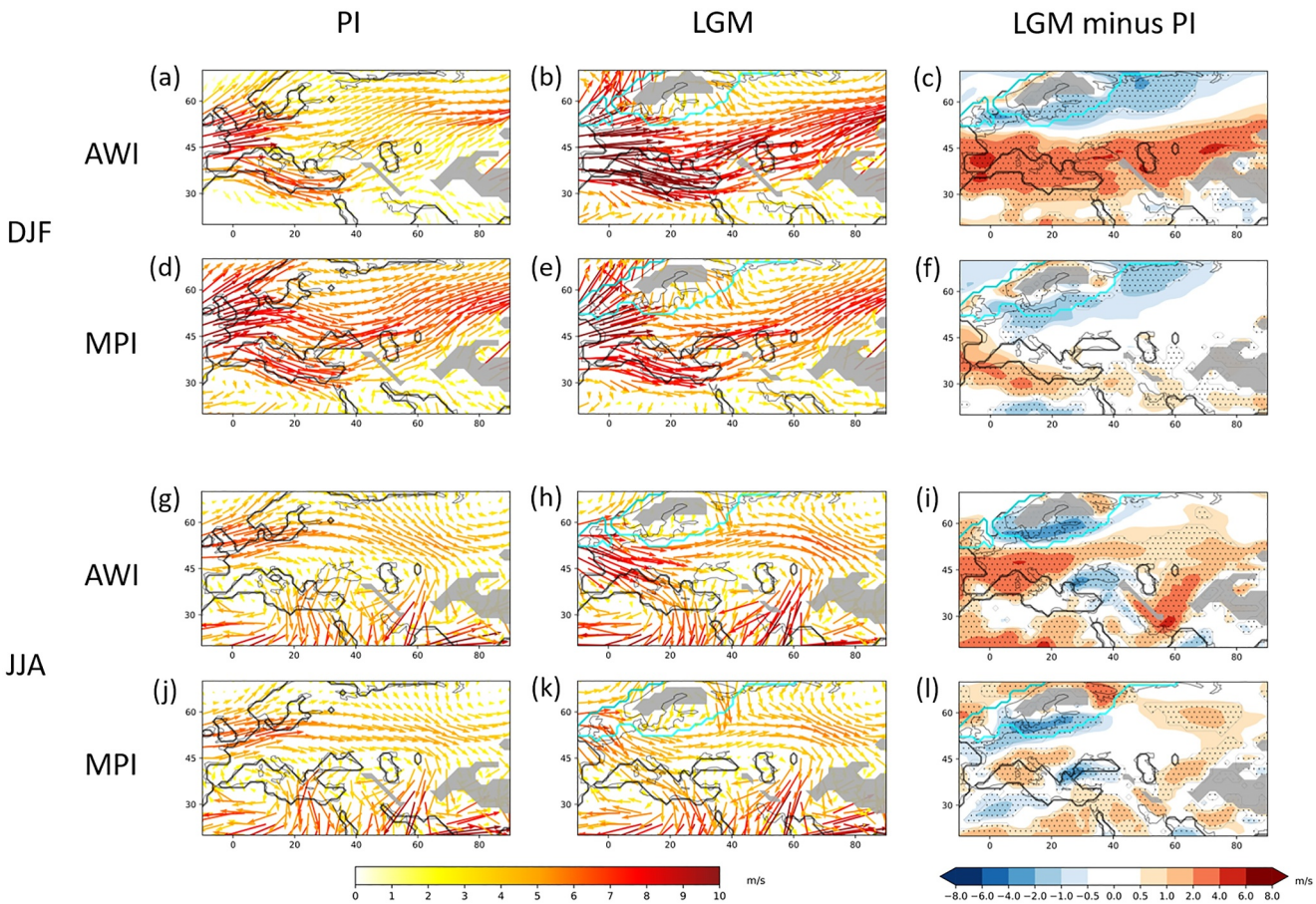


**Figure 5.** Distributions of wind in 850 hPa for winter (a–f) and summer (g–l) as simulated by the AWI and MPI models. Absolute wind vectors of the PI simulations are displayed in the first column, and of the LGM simulations in the second column with color and vector length representing wind speed. LGM minus PI differences are depicted in the third column. Black lines denote the respective implemented coastlines (first column: PI; second and third column: LGM), and cyan lines mark the ice sheet extent during the LGM. Areas with topography higher than 1500 m a.s.l. are masked in gray. Dotted areas indicate a significant change between LGM and PI simulations based on a two-sided bootstrap *t* test at a 99% confidence interval.

the Caspian Sea toward the Elburz Mountains. Except for the anticyclonic CWT over the northern Caspian Sea, summer relative precipitation follows the occurrence frequency distributions, but with only small amounts of precipitation (Figures 6e, 6g, 7e, and 7g). During the LGM, precipitation is generally reduced (see Figure 2 and yearly precipitation sum in Figure S6 in Supporting Information S1). In comparison to PI, winter contributes less to the annual precipitation (see Figure S6 in Supporting Information S1). Additionally, the CWTs are associated with reduced relative precipitation amounts. During winter, the south-westerly CWT is associated with more precipitation according to AWI, while the cyclonic CWT leads to enhanced precipitation in the MPI simulations in the northern Caspian Sea (Figure 7b). Changes for the southern Caspian Sea region are larger (Figure 7d), resulting into reduced relative precipitation for all easterly, northerly and the cyclonic CWT and an (MPI: small) increase for westerly CWTs. Summer precipitation is already low in the Caspian Sea, with further reductions in the north and slight enhancements in the south. However, these changes are minimal (Figures 7f and 7h).

Next, we analyze the characteristics of two exemplary CWTs over the southern Caspian Sea in detail: the cyclonic CWT (see Figures 8 and 9) and the anticyclonic CWT (see Figures 10 and 11). In winter, the cyclonic CWT is characterized by a large negative anomaly of the geopotential height, centered around the southern Caspian Sea and a positive anomaly to the north for both PI and LGM (Figures 8a–8d). Likewise, the center of the negative anomalies is shifted northward and the positive anomalies are weakened during summer (Figures 8e–8h). Although the broad structure in both the PI and the LGM is similar, the negative anomaly is wider and deepened, while the positive anomaly is less pronounced during the LGM (Figure 8, right column). During winter, the cyclonic CWT is associated with large amounts of precipitation, particularly to the south and southwest of the

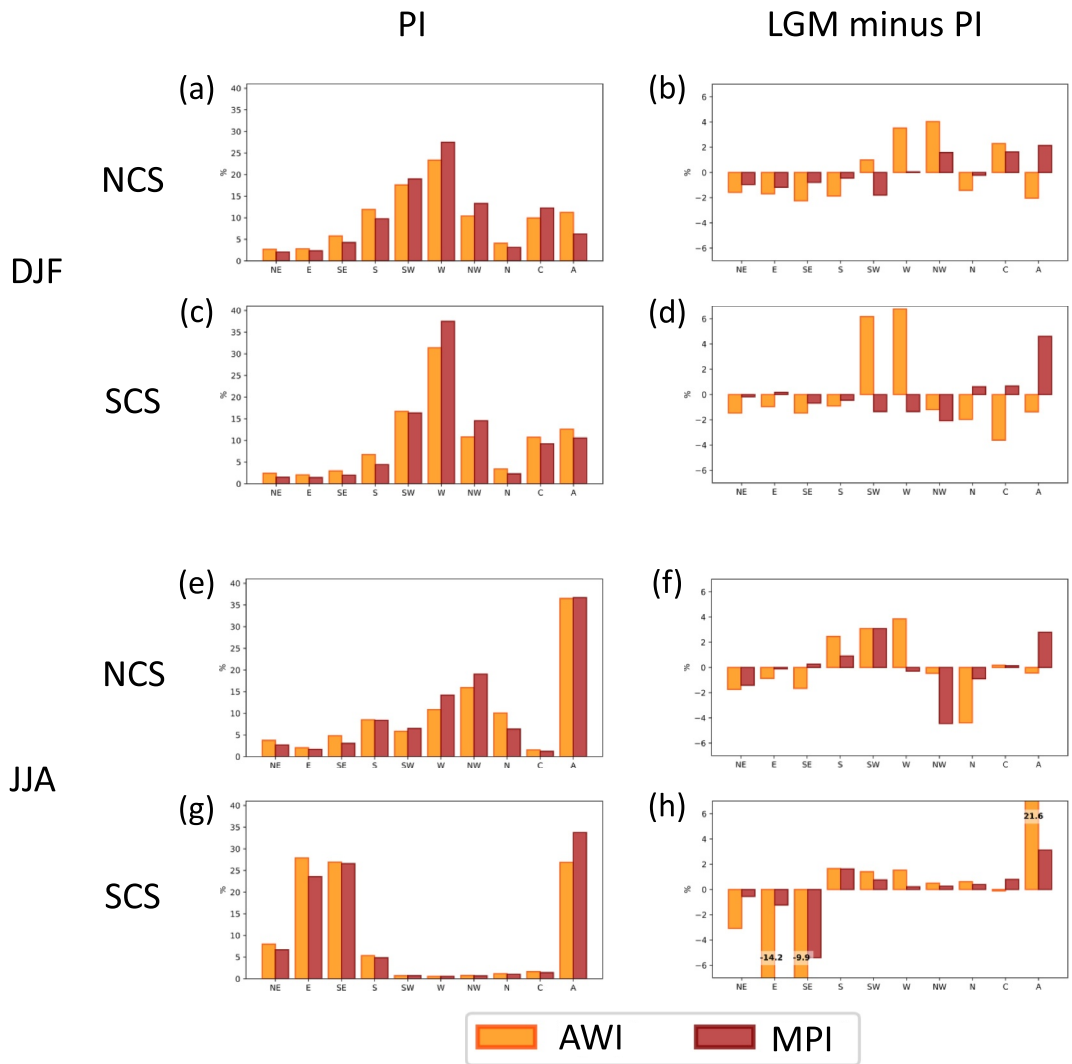


**Figure 6.** CWT frequencies of the northern Caspian Sea (NCS, 46° N; 51° E) and the southern Caspian Sea (SCS, 38° N; 51° E) in winter (a–d) and summer (e–h) based on the AWI simulation (orange bars) and the MPI simulation (red bars). Absolute frequencies of the PI simulations are displayed in the first column; the second column represents LGM minus PI differences.

Caspian Sea (Figures 9a and 9c). However, the summer cyclonic CWT in the PI does not produce any precipitation to the south of the Caspian Sea (Figures 9e and 9g). The simulations from MPI indicate a reduction in winter precipitation south of the Caspian Sea during the LGM (Figure 9d). In contrast, the AWI simulations show a partial increase of winter precipitation in the same region (Figure 9b). Both GCMs indicate a regional increase in summer precipitation (Figures 9f and 9h).

The anticyclonic CWT strongly differs between the two seasons (see Figure 10): During winter, it is characterized by a large positive anomaly over the Caspian Sea, and a slightly negative anomaly over Scandinavia and north of the Caspian Sea for both PI and LGM (Figures 10a–10d). For summer, there is no positive anomaly and only a small and weak negative anomaly northeast of the Caspian Sea (Figures 10e–10h). This is, because the anticyclonic weather type largely reflects the overall summer mean distribution (Figures 6g and 6h and Figure S8 in Supporting Information S1). In the LGM, the respective seasonal differences remain. Again, in winter, there is a strong positive anomaly, which is further broadened and intensified (Figures 10b and 10d). The negative anomaly is shifted northward to the western side of the anticyclonic center, as the Fennoscandian ice sheet blocks the northward circulation. The summer anticyclonic anomalies are similar in the PI and LGM. However, the overall large-scale atmospheric circulation is modified. A stationary anticyclonic circulation is established over the

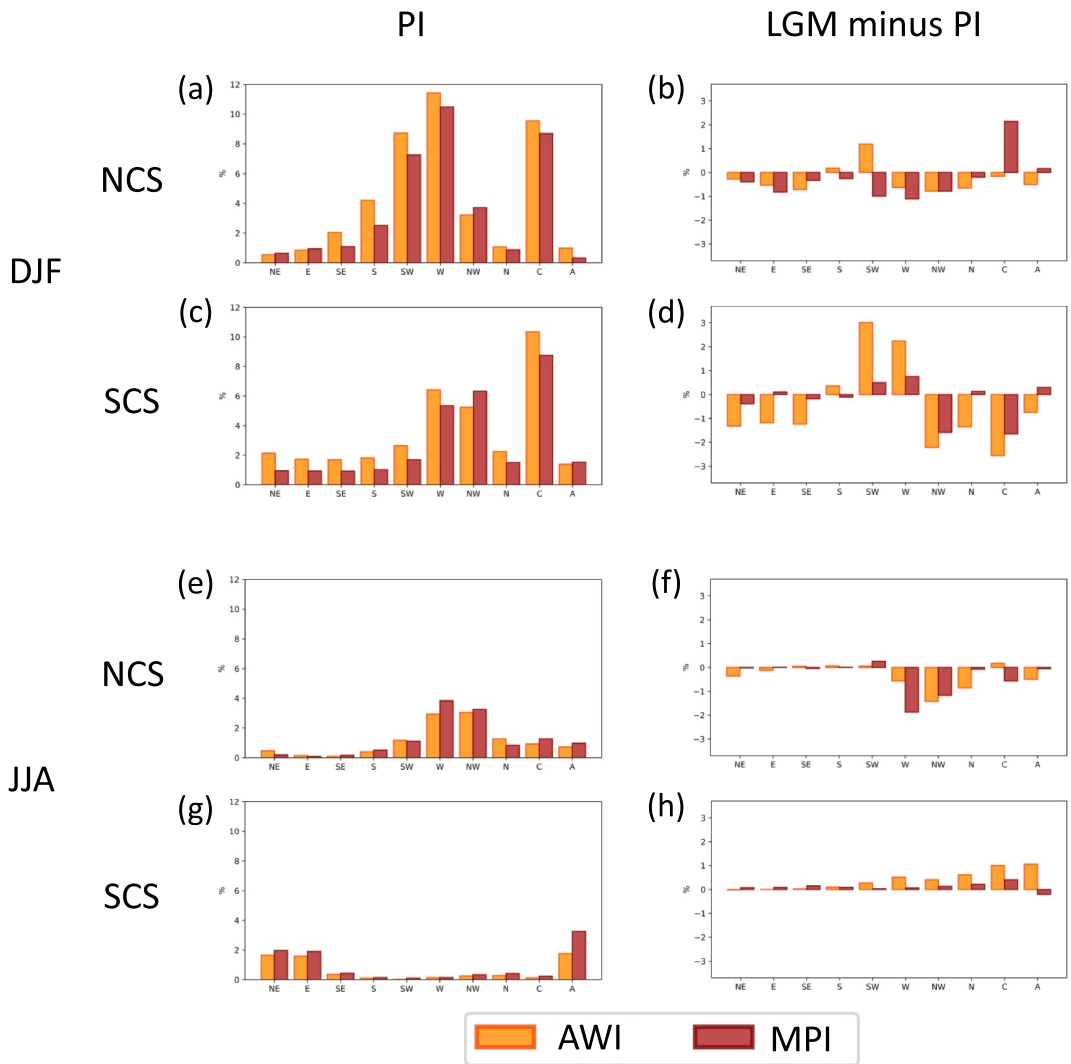


**Figure 7.** Relative annual precipitation per CWT, that is, the relative contributions to the total annual precipitation by each CWT, for the northern Caspian Sea (NCS, 46° N; 51° E) and for the southern Caspian Sea (SCS, 38° N; 51° E) in winter (a–d) and summer (e–h) based on the AWI simulation (orange bars) and the MPI simulation (red bars). Absolute values of the PI simulations are displayed in the first column, and the second column represents LGM minus PI differences.

Fennoscandian ice sheet, so that the large ridge of the PI simulations is modified toward a trough-like pattern over Europe. In both cases, the Caspian Sea is the center of an anticyclonic circulation with almost closed isohypses.

The precipitation associated with the anticyclonic CWT is in general very low over the Caspian Sea (see Figure 11). To the south of the Caspian Sea, there is a pattern with enhanced precipitation in winter (stronger in MPI, see Figures 11a and 11c). However, this pattern is reduced during the LGM (again, more in MPI). In summer, precipitation is restricted to the northern parts—and to a lesser amount west of the Caspian Sea. This precipitation is further reduced during the LGM.

## 4. Discussion and Conclusions

The Caspian Sea region is often ignored in paleoclimate model analyses focusing on Europe and Asia. In this article, we examine the climate of the Caspian Sea region during the LGM and its driving large-scale atmospheric circulation using data from two global climate models within the PMIP4 framework, and focus on three main research avenues. First, we assess how well the climate of the Caspian Sea region is reflected in the climate simulations by comparing them with proxy data from Bartlein et al. (2011). Secondly, we evaluate the changes in

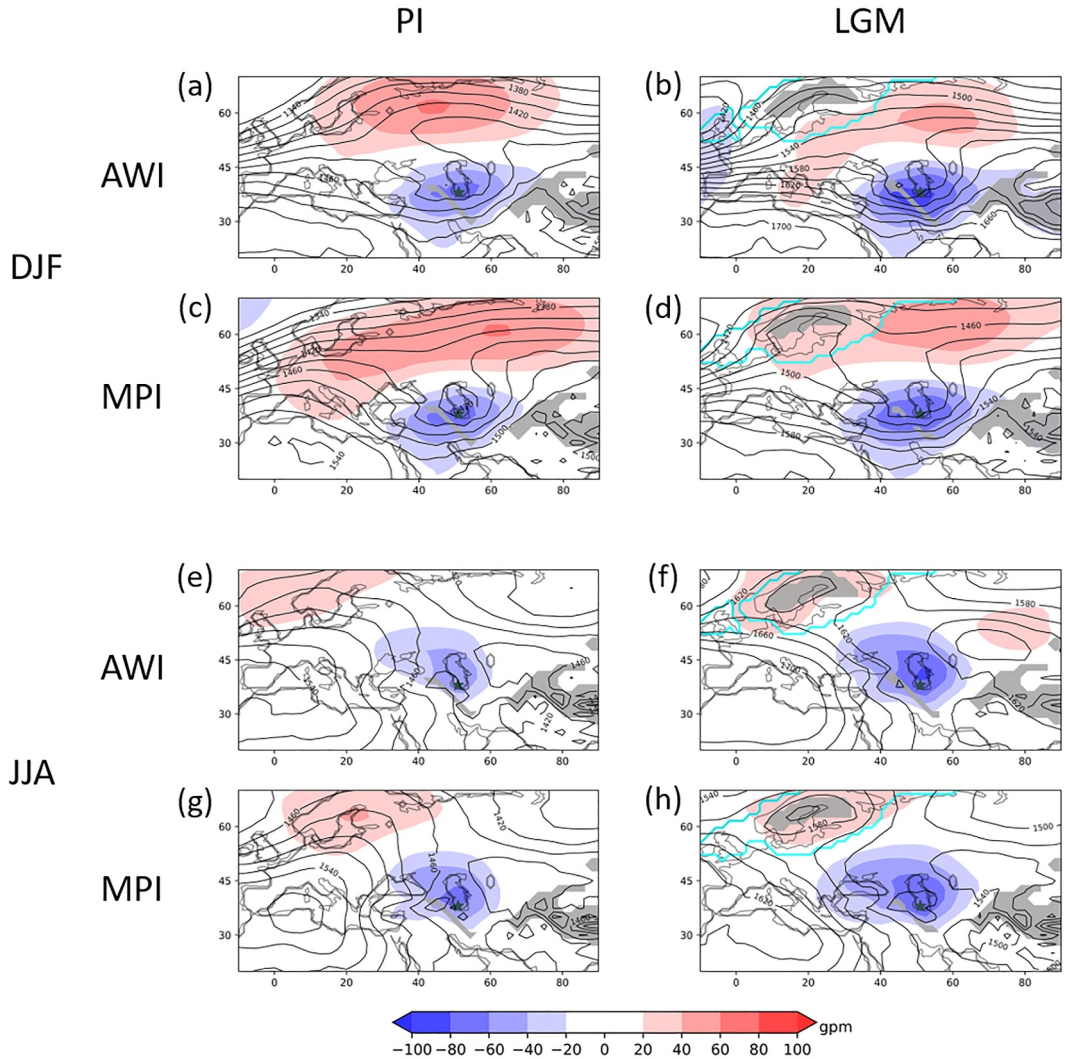


**Figure 8.** Mean geopotential height at 850 hPa for the cyclonic weather type of the southern Caspian Sea in winter (a–d) and summer (e–h) as simulated by the AWI and the MPI models for PI (first column) and for LGM (second column). Absolute fields are displayed as contour lines, and anomalies from the seasonal mean fields are colored. Black lines denote the respective implemented coastlines, and cyan lines mark the ice sheet extent during the LGM. Areas with topography higher than 1500 m a.s.l. are masked in gray. Black stars indicate the location for which the CWT calculation is valid.

the large-scale atmospheric features that drive the climate of the Caspian Sea region from the LGM to the PI, including the 200 hPa jet stream and storm tracks. Lastly, we quantify the regional variations in the near-surface atmospheric circulation during the LGM for two locations in the Caspian Sea region. The discussion is organized in these three research topics.

*How well is the LGM climate of the Caspian Sea region reflected in global climate simulations?*

The general cooling during the LGM is well represented by the simulation data, although there is a discrepancy between the temperatures of the coldest and warmest months and proxy evidence. While the misrepresentation of very cold LGM winter temperatures is a known issue of climate models (e.g., Kageyama et al., 2021; van Ulden & van Oldenborgh, 2006), our results show a better agreement with the proxies in the Pontocaspian Sea region than in Western Europe and the Mediterranean region, especially for the MPI model (cf. Table 1). The quantified precipitation changes align with the direction of change for the proxies in the Pontocaspian Sea region, which is not the case for Western Europe and the Mediterranean region. Notably, the results of the MPI simulations are within the uncertainty range of the proxy data. The results of the AWI model indicate two areas exhibiting positive precipitation anomalies, with one centered over the eastern Anatolian plateau and the other running parallel to

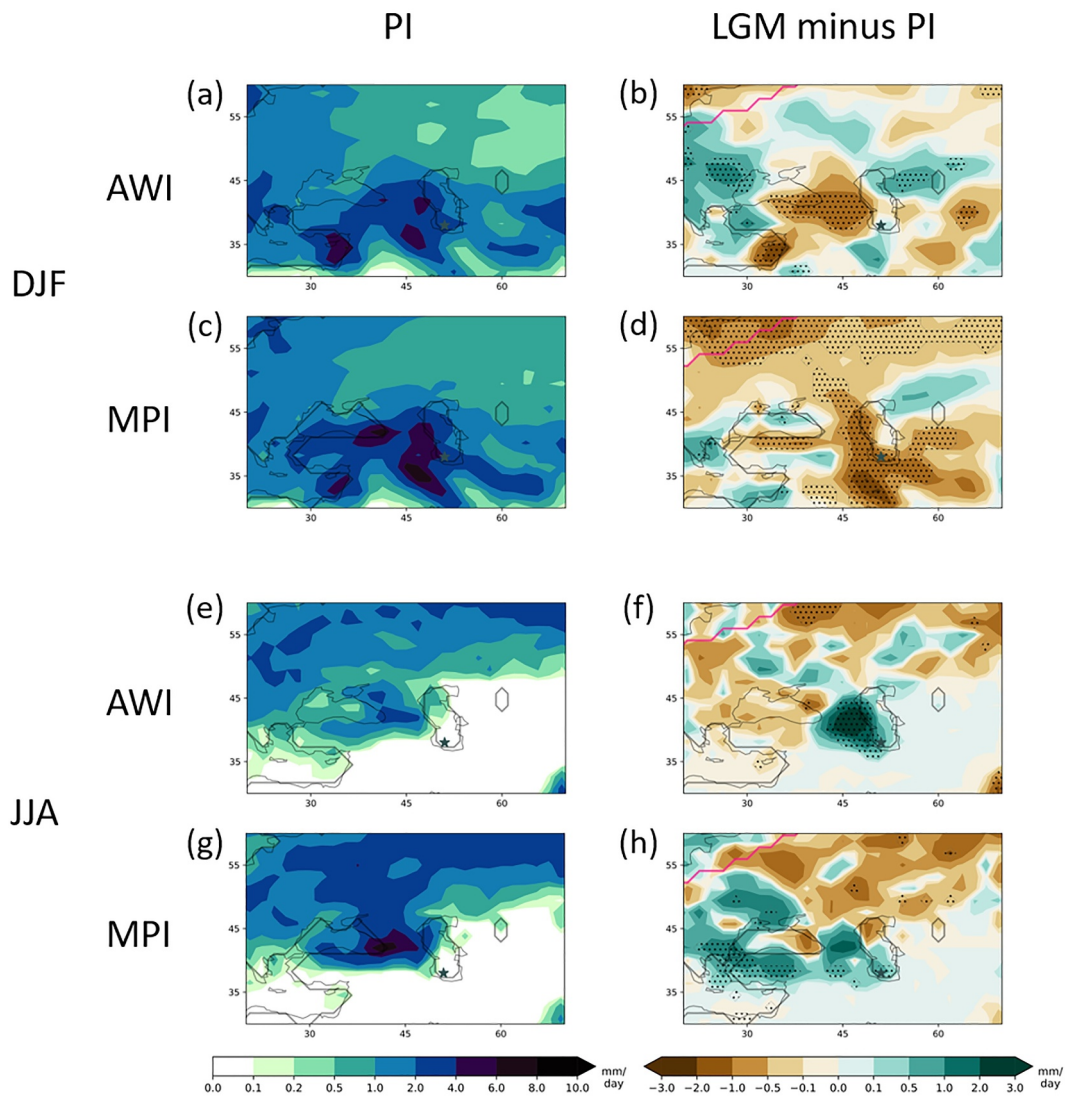


**Figure 9.** Mean daily precipitation associated with the cyclonic weather type for the southern Caspian Sea in winter (a–d) and summer (e–h) as simulated by the AWI and the MPI models. Absolute fields of the PI simulations are displayed in the first column, and the second column represents LGM minus PI differences. Black lines denote the respective implemented coastlines, and pink lines mark the ice sheet extent during the LGM. Dotted areas indicate a significant change between LGM and PI simulations based on a two-sided bootstrap *t* test at a 99% confidence interval. Black stars indicate the location for which the CWT calculation is valid.

45°N from the Western Caucasus toward the central Asian steppes to the northeast of the Caspian Sea. In contrast, the MPI model yielded negative precipitation anomalies for these areas (cf. Figure 2). Paleoclimatic proxy data from Eastern Anatolia rather suggest drier climatic conditions during the LGM than the modern time. The pollen and abiotic records from Lake Van generally show drier climatic conditions during glacials than interglacials (Litt et al., 2014). The stadial phases during glacials, including the LGM, were characterized by dominance of steppe taxa and high clastic input under a sparse vegetation cover, indicating drier conditions than during interstadials (Kwiecien et al., 2014; Pickarski et al., 2015). A similar pattern of minimum continental temperatures during stadials was deduced from Black Sea sediments (Wegwerth et al., 2015), which also document significant changes in pollen assemblages. The latter show a decrease in aridity during the LGM; however, the prevailing climate in the region remained markedly drier than today (Shumilovskikh et al., 2014). Speleothem records from NE Turkey indicate drier winters during the LGM, whereas spring or summer precipitation rates may have been enhanced (Rowe et al., 2012). Further north, speleothems from the Western Caucasus (A. Wolf et al., 2024) indicate a drier LGM with reduced precipitation levels than the present climate. In the southern Caucasus, in an

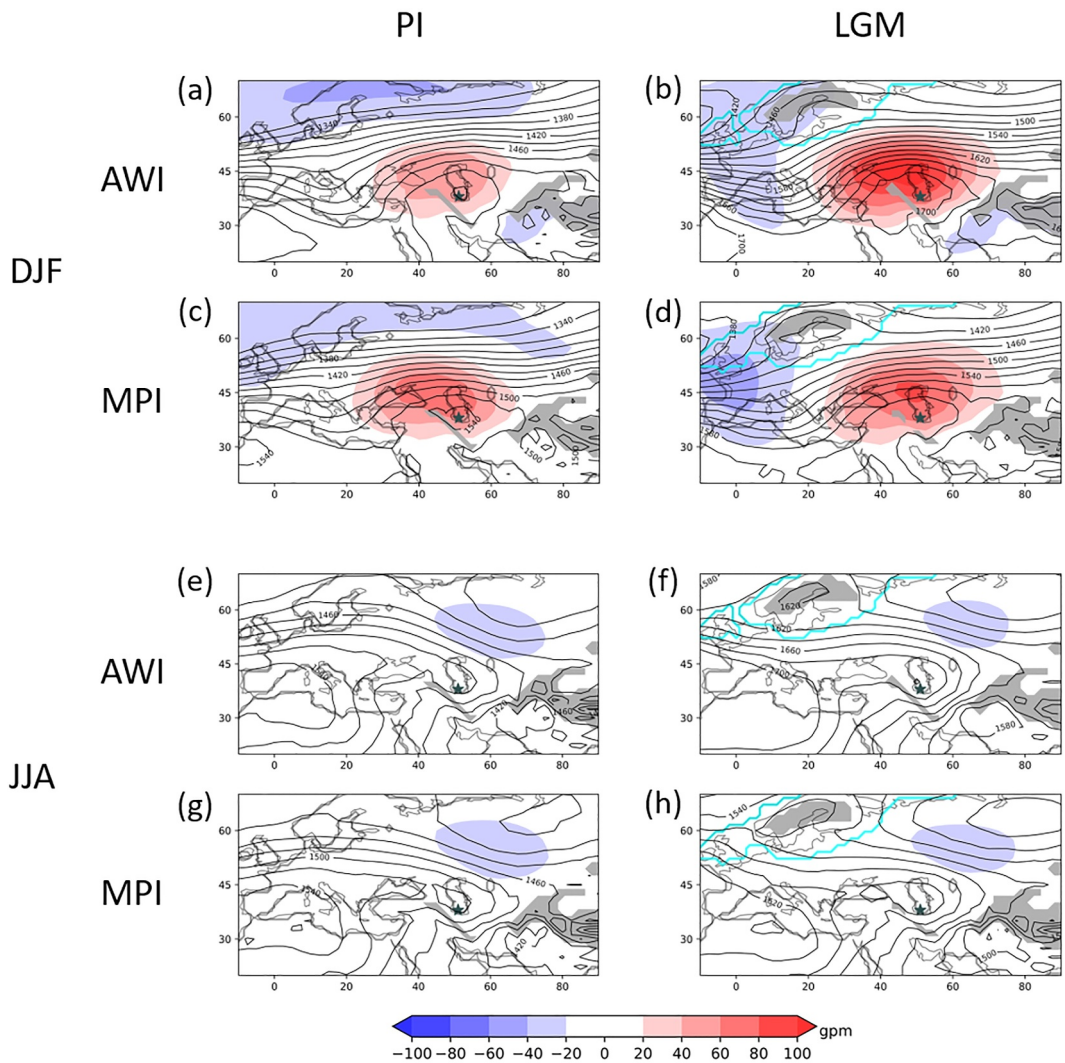


**Figure 10.** Same as Figure 8, but for the anticyclonic weather type.

area exhibiting negative precipitation anomalies in both GCMs, gastropod assemblages from Armenian loess deposits demonstrate that the main dust accumulation phases during the Last Glacial period were characterized by arid climates (e.g., Richter et al., 2020). Intriguingly, dust accumulation rates of Armenian loess deposits during the LGM were apparently very low, which against the background of a lack of erosional discontinuities in the studied sequences, indicate relatively moist conditions during this time (D. Wolf et al., 2022). However, there is also no LGM paleosol in the area, which could indicate a climate similarly moist or even moister than today. It is therefore unlikely that precipitation rates or edaphic moisture were higher during the LGM than they are today. For the lower Volga plains and steppe regions north of the Caspian Sea, paleoclimate records are sparse. Overall, there is no proxy data record that indicates a clearly moister LGM climate than the Holocene in the areas with positive precipitation anomalies simulated by the AWI model.

Similar to Loess deposits in the southern Caspian Sea region (e.g., Frechen et al., 2009; Ghafarpour et al., 2024; Kehl et al., 2021; Vlaminck et al., 2018), pollen in drill cores of the Caspian Sea basin (Leroy et al., 2014) and in the coastal plains of Northern Iran (Leroy et al., 2019) also document a dry and cold Last Glacial Maximum, followed by moist and warm conditions during the Holocene. This trend is also evidenced by pollen records of Lakes Zeribar and Mirabad, both situated in the Zagros Mountains of NW Iran. During the LGM, the pollen assemblage is characterized by a high abundance of Artemisia indicating a dry steppe vegetation in the lake catchments (van Zeist & Bottema, 1991; van Zeist & Wright, 1963). This is in clear contrast to the forest

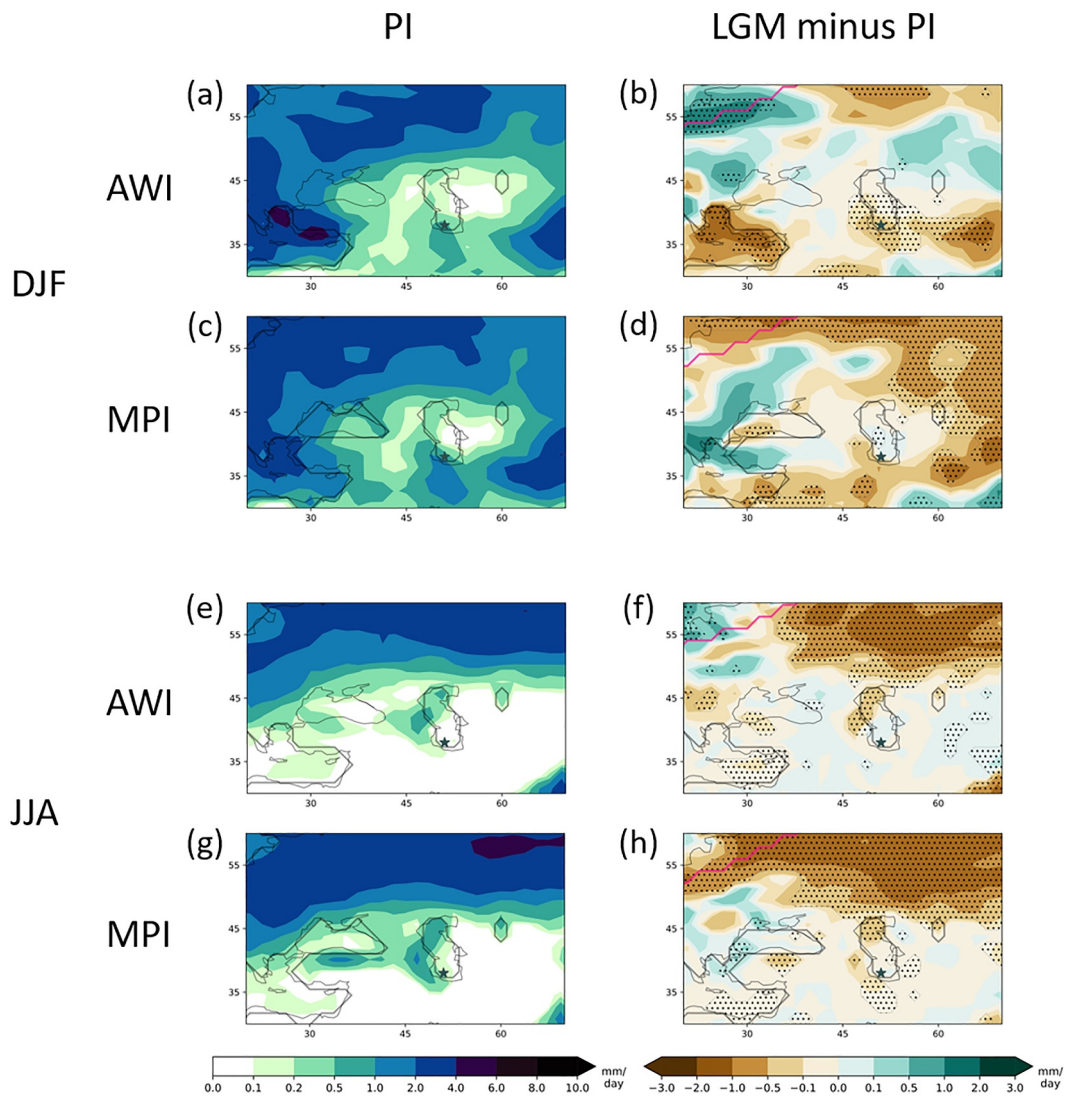


**Figure 11.** Same as Figure 9, but for the anticyclonic weather type.

vegetation types that have been established at least since the middle Holocene. Similarly, the pollen record from Lake Urmia (Djamali et al., 2008) does not suggest any significant moisture-related change during the Late Pleniglacial period, which was characterized by the dominance of Artemisia steppe and a low percentage of arboreal pollen indicating drier conditions than those reconstructed for the Holocene. The reconstruction of lake-level changes of Lake Urmia indicates either constantly low water levels and aridity for the late pleniglacial (Stevens et al., 2012) or a relative highstand between 29 and 20 ka (Kong et al., 2022). These high water levels may have been caused by reduced evaporation or increased precipitation, or a combination of both.

In general, the Pontocaspian region is well represented by the simulation output as deduced from proxy data implications, but differences arise on local scales. Furthermore, our results suggest that the GCM simulations represent the proxy data more accurately in the Caspian Sea region than in the Mediterranean and Western Europe.

*What are the changes in the large-scale atmospheric features that drive the climate of the Caspian Sea region from the LGM to the PI?*

To evaluate what drives the changes in climate conditions from the LGM to the PI, we examined the jet stream characteristics and storm tracks based on the results of the global simulations. We found a dominating subtropical

jet stream in winter with a maximum south of the Caspian Sea, which is reduced in strength during the LGM under enhanced background wind speeds in both climate model simulations. The winter storm track is shifted southward due to the presence of the FIS during the LGM, and the cyclone activity is found to be generally higher. In particular, the AWI model simulations indicate an increased cyclone activity, which could explain the positive precipitation anomalies north of the Caspian Sea. The summer jet stream is located further north than the winter jet stream both during PI and LGM. It changes from a zonal structure during the PI to a wave-like pattern during the LGM with maximum (PI) or minimum (LGM) wind speeds in the Caspian Sea region, leading to a quadrupole structure of LGM to PI differences (see Figures 3f and 3h). These changes can be explained by the presence of the FIS, which acts as a stationary wave-inducing orographic barrier. As such, it deflects the atmospheric flow southward leading to Rossby waves due to the conservation of potential vorticity (e.g., Rossby et al., 1939; Hoskins & Karoly, 1981, for the general theoretical background). Merz et al. (2015) showed this relationship for variable heights of the Laurentide Ice Sheet during the LGM. The theory can also applied to FIS, which influences the jet stream to follow a wave-like structure in the Pontocaspian region.

At the surface, strong westerlies from the North Atlantic and the Mediterranean Sea dominate the circulation in winter during PI conditions. The winds are stronger in the MPI simulation than in the AWI simulation under PI conditions. However, changes toward higher wind speeds during the LGM are more pronounced in the AWI simulations. Higher intensities of surface winds during the winter would promote aeolian dynamics involving the deflation of sediment grains from alluvial plains and the accumulation of loess in neighboring areas such as the Iranian loess plateau or the northern declivity of the Alborz Mountains. In these areas, increased dust accumulation rates during MIS 4 to MIS 2 compared to MIS 1 indicates that wind intensities were stronger under a drier climate than today (e.g., Frechen et al., 2009; Ghafarpour et al., 2024; Kehl et al., 2021; Lauer, Frechen, et al., 2017; Lauer, Vlaminck, et al., 2017; Vlaminck et al., 2018).

*What are the regional variations in the near-surface atmospheric circulation during the LGM in the Caspian Sea region?*

Over the southern Caspian Sea, a shift in the flow regime from westerly and rotational to easterly and anticyclonic flow is observed between winter and summer. Anticyclonic circulation dominates in summer and becomes even more frequent during the LGM. Conversely, easterly winds become less frequent over both the northern and southern Caspian Sea and coherently in both models. Furthermore, summer westerly winds are weaker than in winter and turn to northerly winds east of the Caspian Sea.

Deriving paleowind directions from loess deposits has not been a common undertaking, yet there is some information available regarding the probable source areas of the dust, which can be used as indirect evidence for wind direction (Ghafarpour et al., 2024; Kehl, 2010; Költringer et al., 2022; Wang et al., 2017). The dust sources are located in the west and the north of the dust accumulation areas. It is thus very likely that westerly and northerly winds were responsible for the accumulation of loess in Northern Iran, as previously suggested by Lateef (1988).

In accordance with the generally drier climate during the LGM, most circulation types are associated with reduced precipitation in both seasons. The relative contribution of winter precipitation is decreased during the LGM, except for westerly (southern and northern Caspian Sea, AWI model) and cyclonic CWTs (northern Caspian Sea, MPI model). The moisture source of the precipitation might therefore be the North Atlantic or Mediterranean Sea. A continental moisture source seems unlikely according to our CWT analysis. The contribution of easterly flow types to the annual precipitation is very low during the PI and is further reduced during the LGM.

The changes in characteristics of the CWTs between PI and LGM are analyzed in detail, with a particular focus on the cyclonic and anticyclonic circulation types over the Caspian Sea. During the LGM, the anomalies of the geopotential height feature an intensification, accompanied by broadening and deepening of the anomaly centers compared to the PI. The winter anticyclonic CWT anomalies exhibit a shift in pattern from a north-south dipole during the PI to a west-east dipole due to the influence of the FIS during the LGM.

The summer cyclonic CWT is associated with more regional precipitation during the LGM, but occurrence frequencies remain low. The models disagree in terms of winter cyclonic precipitation over the southern Caspian Sea.

In general, the agreement between the models is better on a larger scale perspective. The MPI model shows stronger winds and more precipitation in the PI simulation. However, the changes during the LGM are less pronounced than those depicted in the AWI model simulations. The AWI simulations show a stronger jet evolving over the continent and favoring a continuous and stronger storm track in winter. This can explain the enhanced precipitation band over the Caucasus and north of the Black and Caspian Seas, and partly also the positive precipitation anomaly over the eastern Anatolian plateau (see Figure 2f). Data from single pollen sites suggest a drier climate than today, agreeing with the MPI model for annual mean precipitation, but may nevertheless reveal enhanced precipitation in summer (Rowe et al., 2012). This enhanced summer precipitation maybe explained by the anomaly pattern of the cyclonic weather type during the LGM for the southern Caspian Sea (see Figure 9f). The cyclonic weather type does not occur frequently, but is associated with a strong positive precipitation anomaly in the area of the eastern Anatolian plateau. For the southern Caspian Sea region, both models simulate a drier climate in line with proxy evidence. This can be associated with the southward shift of the winter jet, leading to less influence of the jet on the region with generally reduced jet wind speeds. Nevertheless, westerly circulation types dominate in winter together with anticyclonic atmospheric flow (esp. MPI). This is in agreement with the inferred wind direction from dust source analysis, although the models partly contradict in their simulated changes of prevailing atmospheric flow types.

Some of the discrepancies observed in the Caspian Sea region maybe attributed to the different implementations of the Black Sea, which is not part of the ocean model for AWI simulations. This may, for example, explain the different precipitation patterns associated with the cyclonic weather type over the Caspian Sea, where the MPI simulations indicate more precipitation than the AWI simulations. Besides this, deviations from proxy evidence can be attributed to two main factors. Firstly, the Caspian Sea is implemented with the water level of today, which is −27 m and a corresponding size of the lake. However, already during the last 100 years, the Caspian Sea level varied by more than 3 m. These changes of the water level are influenced by teleconnection patterns, mainly ENSO and to a lesser extent the NAO (e.g., Lahijani et al., 2023; Molavi-Arabshahi & Arpe, 2022) and have an impact on the atmospheric circulation, Caspian Sea surface temperatures, and wind variability according to several studies (Arpe et al., 2020; Koriche et al., 2021; Lahijani et al., 2023; Serykh & Kostianoy, 2020). Koriche et al. (2021) showed, for example, that summer (winter) air temperatures are reduced (enhanced) with a larger Caspian Sea, and precipitation amounts are increased over central Asia. In timescales of 10–100 thousands of years, the Caspian Sea underwent multiple transgression and regression phases with amplitudes of more than 100 m. As a result, there is still a lack of consensus regarding the precise water level of the Caspian Sea during the LGM, due to the presence of conflicting proxy evidence (e.g., Krijgsman et al., 2019; Tudryn et al., 2022). Secondly, the horizontal resolution of the global paleoclimate models (∼200 km) is much coarser than the resolution of the very local proxy data.

In order to gain insight into the regional climate of the Caspian Sea region during the LGM, it is essential to conduct sensitivity studies with high-resolution regional climate model simulations. The coarse resolution of the global climate models cannot capture the complex topography, especially in the southern Caspian Sea region, adequately. Neither the steep slopes from the Caspian Sea below sea level to the highest peaks of the Elburz Mountains, nor the height of those and the Caucasus Mountains can be appropriately represented at a horizontal resolution of ∼200 km. While in reality the highest peaks in these mountain ranges have a height of approximately 5 km, the model topography is limited to less than 2 km in this area. The representation of the topography is inherently improved by higher resolution simulations. In addition, there exist many loess profiles, particularly in the southern Caspian Sea region (e.g., Ghafarpour et al., 2024; Kehl et al., 2021), where high-resolution regional climate modeling enables to bridge the gap between coarse global climate model data and local proxy data (Ludwig et al., 2019). Increasing the model resolution generally also improves the representation of physical processes that govern regional precipitation patterns (such as orographic precipitation) and amounts, in particular, when it comes with complex topography. This has been shown in various studies for the present day (e.g., Feser et al., 2011; Jacob et al., 2014), and has also been proven to be beneficial under paleoclimate conditions (e.g., Ludwig et al., 2019; Zheng et al., 2004). Furthermore, the climate of the Caspian Sea region is also largely influenced by the size of the Caspian Sea. An illustrative example of a sensitivity study is conducted by Koriche et al. (2021), where they test the impact of different Caspian Sea water level on the catchment-scale and large-scale climate by using a global climate model under PI conditions. Therefore, future work should combine high-resolution regional climate modeling under LGM conditions and focus on the impact of the Caspian Sea

water levels on the regional hydroclimate during the LGM, allowing for a more accurate model-proxy comparison.

## Data Availability Statement

The basis of this study are global climate model simulations from the Coupled Model Intercomparison Project Phase 6 (CMIP6, Eyring et al., 2016)/Paleoclimate Modelling Intercomparison Project Phase 4 (PMIP4, Kageyama et al., 2017) framework. We used data of the piControl and LGM experiments of the AWI-ESM-1-1LR model (Danek et al., 2020; Shi et al., 2020, respectively) and of the MPI-ESM1.2-LR model (Jungclaus et al., 2019; Wieners et al., 2019, respectively). The climate model data are openly available via the Earth System Gridded Federation (ESGF) Nodes (https://esgf-metagrid.cloud.dkrz.de/). The quantitative model-proxy comparison is compiled with proxy data published in Bartlein et al. (2011). Topography data that were used in Figure 1 are openly available at NOAA (2022).

**Acknowledgments**
KHS and JGP thank the AXA Research Fund for support. PL is supported by the Helmholtz "Changing Earth" program. This work used resources of the Deutsches Klimarechenzentrum (DKRZ) granted by its Scientific Steering Committee (WLA) under project ID 965. The constructive comments of four anonymous reviewers are gratefully acknowledged. Open Access funding enabled and organized by Projekt DEAL.

## References

Akçar, N., & Schlüchter, C. (2005). Paleoglaciations in Anatolia: A schematic review and first results. *Eiszeitalter und Gegenwart E&G/Quaternary Science Journal*, *55*(1), 102–121. https://doi.org/10.7892/boris.47000

Amaya, D. J., Seltzer, A. M., Karnauskas, K. B., Lora, J. M., Zhang, X., & DiNezio, P. N. (2022). Air-sea coupling shapes North American hydroclimate response to ice sheets during the Last Glacial Maximum. *Earth and Planetary Science Letters*, *578*, 117271. https://doi.org/10.1016/j.epsl.2021.117271

Annan, J. D., & Hargreaves, J. C. (2013). A new global reconstruction of temperature changes at the Last Glacial Maximum. *Climate of the Past*, *9*(1), 367–376. https://doi.org/10.5194/cp-9-367-2013

Antoine, P., Bahain, J.-J., Berillon, G., & Asgari Khaneghan, A. (2006). Tuf calcaire et séquence alluviale en contexte tectonique actif: la formation de baliran (province du Mazadaran, Iran). *Quaternaire*, *17*(4), 321–331. https://doi.org/10.4000/quaternaire.891

Arpe, K., Molavi-Arabshahi, M., & Leroy, S. (2020). Wind variability over the Caspian Sea, its impact on Caspian seawater level and link with ENSO. *International Journal of Climatology*, *40*(14), 6039–6054. https://doi.org/10.1002/joc.6564

Bartlein, P. J., Harrison, S. P., Brewer, S., Connor, S., Davis, B. A. S., Gajewski, K., et al. (2011). Pollen-based continental climate reconstructions at 6 and 21 ka: A global synthesis. *Climate Dynamics*, *37*(3), 775–802. https://doi.org/10.1007/s00382-010-0904-1

Clark, P. U., Dyke, A. S., Shakun, J. D., Carlson, A. E., Clark, J., Wohlfarth, B., et al. (2009). The Last Glacial Maximum. *Science*, *325*(5941), 710–714. https://doi.org/10.1126/science.1172873

Danek, C., Shi, X., Stepanek, C., Yang, H., Barbi, D., Hegewald, J., & Lohmann, G. (2020). AWI AWI-ESM1.1LR model output prepared for CMIP6 CMIP piControl [Dataset]. *Earth System Grid Federation*. https://doi.org/10.22033/ESGF/CMIP6.9335

Djamali, M., de Beaulieu, J.-L., Shah-hosseini, M., Andrieu-Ponel, V., Ponel, P., Amini, A., et al. (2008). A late pleistocene long pollen record from Lake Urmia, NW Iran. *Quaternary Research*, *69*(3), 413–420. https://doi.org/10.1016/j.yqres.2008.03.004

Dolukhanov, P. M., Chepalyga, A. L., & Lavrentiev, N. V. (2010). The Khvalynian transgressions and early human settlement in the Caspian Basin. *Quaternary International*, *225*(2), 152–159. (Caspian–Black Sea–Mediterranean Corridors during the Last 30 ka: Sea Level Change and Human Adaptive Strategies). https://doi.org/10.1016/j.quaint.2009.10.039

Eyring, V., Bony, S., Meehl, G. A., Senior, C. A., Stevens, B., Stouffer, R. J., & Taylor, K. E. (2016). Overview of the coupled model intercomparison project phase 6 (CMIP6) experimental design and organization. *Geoscientific Model Development*, *9*(5), 1937–1958. https://doi.org/10.5194/gmd-9-1937-2016

Feser, F., Rockel, B., von Storch, H., Winterfeldt, J., & Zahn, M. (2011). Regional climate models add value to global model data: A review and selected examples. *Bulletin of the American Meteorological Society*, *92*(9), 1181–1192. https://doi.org/10.1175/2011BAMS3061.1

Frechen, M., Kehl, M., Rolf, C., Sarvati, R., & Skowronek, A. (2009). Loess chronology of the Caspian lowland in northern Iran. *Quaternary International*, *198*(1), 220–233. (Loess in the Danube Region and Surrounding Loess Provinces: The Marsigli Memorial Volume). https://doi.org/10.1016/j.quaint.2008.12.012

Ghafarpour, A., Khormali, F., Tazikeh, H., Kehl, M., Frechen, M., & Zolitschka, B. (2024). Loess origin and late Pleistocene environmental reconstruction for northeastern Iran: Multiproxy evidences from the Chenarli loess-paleosol sequence. *Quaternary Science Reviews*, *328*, 108545. https://doi.org/10.1016/j.quascirev.2024.108545

Haghani, S., & Leroy, S. A. (2020). Recent avulsion history of Sefidrud, South West of the Caspian Sea. *Quaternary International*, *540*, 97–110. https://doi.org/10.1016/j.quaint.2018.06.034

Hoskins, B. J., & Karoly, D. J. (1981). The steady linear response of a spherical atmosphere to thermal and orographic forcing. *Journal of the Atmospheric Sciences*, *38*(6), 1179–1196. https://doi.org/10.1175/1520-0469(1981)038⟨1179:TSLROA⟩2.0.CO;2

Hoskins, B. J., & Valdes, P. J. (1990). On the existence of storm-tracks. *Journal of the Atmospheric Sciences*, *47*(15), 1854–1864. https://doi.org/10.1175/1520-0469(1990)047⟨1854:OTEOST⟩2.0.CO;2

Izumi, K., Valdes, P., Ivanovic, R., & Gregoire, L. (2023). Impacts of the PMIP4 ice sheets on northern hemisphere climate during the last glacial period. *Climate Dynamics*, *60*(7–8), 2481–2499. https://doi.org/10.1007/s00382-022-06456-1

Jacob, D., Petersen, J., Eggert, B., Alias, A., Christensen, O. B., Bouwer, L. M., et al. (2014). EURO-CORDEX: New high-resolution climate change projections for European impact research. *Regional Environmental Change*, *14*(2), 563–578. https://doi.org/10.1007/s10113-013-0499-2

Jones, P. D., Hulme, M., & Briffa, K. R. (1993). A comparison of lamb circulation types with an objective classification scheme. *International Journal of Climatology*, *13*(6), 655–663. https://doi.org/10.1002/joc.3370130606

Jouvet, G., Cohen, D., Russo, E., Buzan, J., Raible, C. C., Haeberli, W., et al. (2023). Coupled climate-glacier modelling of the last glaciation in the alps. *Journal of Glaciology*, *69*(278), 1956–1970. https://doi.org/10.1017/jog.2023.74

Jungclaus, J., Mikolajewicz, U., Kapsch, M.-L., D'Agostino, R., Wieners, K.-H., Giorgetta, M., et al. (2019). MPI-M MPI-ESM1.2-LR model output prepared for CMIP6 PMIP LGM [Dataset]. *Earth System Grid Federation*. https://doi.org/10.22033/ESGF/CMIP6.6642

Justino, F., & Peltier, W. R. (2005). The glacial north Atlantic Oscillation. *Geophysical Research Letters*, *32*(21), L21803. https://doi.org/10.1029/2005GL023822

Kageyama, M., Albani, S., Braconnot, P., Harrison, S. P., Hopcroft, P. O., Ivanovic, R. F., et al. (2017). The PMIP4 contribution to CMIP6—Part 4: Scientific objectives and experimental design of the PMIP4-CMIP6 Last Glacial Maximum experiments and PMIP4 sensitivity experiments. *Geoscientific Model Development*, *10*(11), 4035–4055. https://doi.org/10.5194/gmd-10-4035-2017

Kageyama, M., Harrison, S. P., Kapsch, M.-L., Lofverstrom, M., Lora, J. M., Mikolajewicz, U., et al. (2021). The PMIP4 Last Glacial Maximum experiments: Preliminary results and comparison with the PMIP3 simulations. *Climate of the Past*, *17*(3), 1065–1089. https://doi.org/10.5194/cp-17-1065-2021

Kalugin, A., & Morozova, P. (2023). Hydrometeorological conditions of the Volga flow generation into the Caspian Sea during the Last Glacial Maximum. *Climate*, *11*(2), 36. https://doi.org/10.3390/cli11020036

Kehl, M. (2010). *Quarternary loesses, loess-like sediments, soils and climate change in Iran*. Borngraeger. Berlin.

Kehl, M., Vlaminck, S., Köhler, T., Laag, C., Rolf, C., Tsukamoto, S., et al. (2021). Pleistocene dynamics of dust accumulation and soil formation in the southern Caspian Lowlands—New insights from the loess-paleosol sequence at Neka-Abelou, northern Iran. *Quaternary Science Reviews*, *253*, 106774. https://doi.org/10.1016/j.quascirev.2020.106774

Klige, R. K., & Myagkov, M. S. (1992). Changes in the water regime of the Caspian Sea. *Geojournal*, *27*(3), 299–307. https://doi.org/10.1007/BF02482671

Költringer, C., Stevens, T., Lindner, M., Baykal, Y., Ghafarpour, A., Khormali, F., et al. (2022). Quaternary sediment sources and loess transport pathways in the black sea—Caspian sea region identified by detrital zircon U-Pb geochronology. *Global and Planetary Change*, *209*, 103736. https://doi.org/10.1016/j.gloplacha.2022.103736

Kong, T., Tudryn, A., Gibert-Brunet, E., Tucholka, P., Motavalli-Anbaran, S.-H., Ahmady-Birgani, H., et al. (2022). 30,000 years of the southwestern lake Urmia (Iran) paleoenvironmental evolution inferred from mineralogical indicators from lake and watershed sediments. *Journal of Asian Earth Sciences*, *239*, 105387. https://doi.org/10.1016/j.jseaes.2022.105387

Koriche, S. A., Nandini-Weiss, S. D., Prange, M., Singarayer, J. S., Arpe, K., Cloke, H. L., et al. (2021). Impacts of variations in Caspian Sea surface area on catchment-scale and large-scale climate. *Journal of Geophysical Research: Atmospheres*, *126*(18), e2020JD034251. https://doi.org/10.1029/2020JD034251

Kosarev, A. (2005). Physico-geographical conditions of the Caspian Sea. In A. Kostianoy & A. Kosarev (Eds.), *The Caspian Sea environment*, *The handbook of environmental chemistry* (Vol. 5P, pp. 5–31). Springer. Berlin, Heidelberg. https://doi.org/10.1007/698_5_002

Kosarev, A., Kostianoy, A. G., Zonn, I. S., & Zhiltsov, S. S. (2014). The Caspian Sea and Kara-Bogaz-Gol Bay. In I. S. Zonn & A. G. Kostianoy (Eds.), *The Turkmen Lake Altyn Asyr and water resources in Turkmenistan* (pp. 69–94). Springer Berlin Heidelberg. https://doi.org/10.1007/698_2013_228

Krijgsman, W., Tesakov, A., Yanina, T., Lazarev, S., Danukalova, G., Van Baak, C., et al. (2019). Quaternary time scales for the pontocaspian domain: Interbasinal connectivity and faunal evolution. *Earth-Science Reviews*, *188*, 1–40. https://doi.org/10.1016/j.earscirev.2018.10.013

Kwiecien, O., Stockhecke, M., Pickarski, N., Heumann, G., Litt, T., Sturm, M., et al. (2014). Dynamics of the last four glacial terminations recorded in Lake Van, Turkey. *Quaternary Science Reviews*, *104*, 42–52. https://doi.org/10.1016/j.quascirev.2014.07.001

Lahijani, H., Leroy, S., Arpe, K., & Crétaux, J.-F. (2023). Caspian sea level changes during instrumental period, its impact and forecast: A review. *Earth-Science Reviews*, *241*, 104428. https://doi.org/10.1016/j.earscirev.2023.104428

Lambeck, K., Rouby, H., Purcell, A., Sun, Y., & Sambridge, M. (2014). Sea level and global ice volumes from the last glacial maximum to the Holocene. *Proceedings of the National Academy of Sciences of the United States of America*, *111*(43), 15296–15303. https://doi.org/10.1073/pnas.1411762111

Lateef, A. (1988). Distribution, provenance, age and paleoclimatic record of the loess in central north Iran. In D. Eden & R. Furkert (Eds.), *Loess—lts distribution, geology and soils* (pp. 93–101). Balkema. Rotterdam.

Lauer, T., Frechen, M., Vlaminck, S., Kehl, M., Lehndorff, E., Shahriari, A., & Khormali, F. (2017). Luminescence-chronology of the loess palaeosol sequence toshan, northern Iran—A highly resolved climate archive for the last glacial–interglacial cycle. *Quaternary International*, *429*(Part B), 3–12. https://doi.org/10.1016/j.quaint.2015.03.045

Lauer, T., Vlaminck, S., Frechen, M., Rolf, C., Kehl, M., Sharifi, J., et al. (2017). The AGH band loess-palaeosol sequence—A terrestrial archive for climatic shifts during the last and penultimate glacial–interglacial cycles in a semiarid region in northern Iran. *Quaternary International*, *429*, 13–30. https://doi.org/10.1016/j.quaint.2016.01.062

Lei, J., Shi, Z., Xie, X., Sha, Y., Li, X., Liu, X., & An, Z. (2021). Seasonal variation of the westerly jet over Asia in the Last Glacial Maximum: Role of the Tibetan Plateau heating. *Journal of Climate*, *34*(7), 2723–2740. https://doi.org/10.1175/JCLI-D-20-0438.1

Leroy, S., Amini, A., Gregg, M., Marinova, E., Bendrey, R., Zha, Y., et al. (2019). Human responses to environmental change on the southern coastal plain of the Caspian Sea during the mesolithic and neolithic periods. *Quaternary Science Reviews*, *218*, 343–364. https://doi.org/10.1016/j.quascirev.2019.06.038

Leroy, S., López-Merino, L., Tudryn, A., Chalié, F., & Gasse, F. (2014). Late pleistocene and Holocene palaeoenvironments in and around the middle Caspian Basin as reconstructed from a deep-sea core. *Quaternary Science Reviews*, *101*, 91–110. https://doi.org/10.1016/j.quascirev.2014.07.011

Li, C., & Battisti, D. S. (2008). Reduced Atlantic storminess during Last Glacial Maximum: Evidence from a coupled climate model. *Journal of Climate*, *21*(14), 3561–3579. https://doi.org/10.1175/2007JCLI2166.1

Litt, T., Pickarski, N., Heumann, G., Stockhecke, M., & Tzedakis, P. (2014). A 600,000 year long continental pollen record from Lake Van, eastern Anatolia (Turkey). *Quaternary Science Reviews*, *14*, 30–41. (Special Issue: Results from the PALEOVAN Drilling Project: a 600,000 year long continental archive in the Near East). https://doi.org/10.1016/j.quascirev.2014.03.017

Löfverström, M., Caballero, R., Nilsson, J., & Kleman, J. (2014). Evolution of the large-scale atmospheric circulation in response to changing ice sheets over the last glacial cycle. *Climate of the Past*, *10*(4), 1453–1471. https://doi.org/10.5194/cp-10-1453-2014

Lohmann, G., Butzin, M., Eissner, N., Shi, X., & Stepanek, C. (2020). Abrupt climate and weather changes across time scales. *Paleoceanography and Paleoclimatology*, *35*(9), e2019PA003782. https://doi.org/10.1029/2019PA003782

Lu, F., Gu, Y., Lin, P., Lu, Z., Zhang, H., an Zhang, Q., et al. (2025). Tipping point-induced abrupt shifts in east Asian hydroclimate since the last glacial maximum. *Nature Communications*, *16*(477), 477. https://doi.org/10.1038/s41467-025-55888-w

Ludwig, P., Gómez-Navarro, J. J., Pinto, J. G., Raible, C. C., Wagner, S., & Zorita, E. (2019). Perspectives of regional paleoclimate modeling. *Annals of the New York Academy of Sciences*, *1436*(1), 54–69. https://doi.org/10.1111/nyas.13865

Ludwig, P., Pinto, J. G., Raible, C. C., & Shao, Y. (2017). Impacts of surface boundary conditions on regional climate model simulations of European climate during the Last Glacial Maximum. *Geophysical Research Letters*, *44*(10), 5086–5095. https://doi.org/10.1002/2017GL073622

Ludwig, P., Schaffernicht, E. J., Shao, Y., & Pinto, J. G. (2016). Regional atmospheric circulation over Europe during the last glacial maximum and its links to precipitation. *Journal of Geophysical Research: Atmospheres*, *121*(5), 2130–2145. https://doi.org/10.1002/2015JD024444

Maleki, S., Khormali, F., Kehl, M., Azizi, G., Shahpouri, F., Shahbazi, R., & Frechen, M. (2023). A loess-paleosol record of climate and vegetation change during the past 27,000 years from south-east of the Caspian Sea, Iran. *Quaternary International*, *652*, 1–16. https://doi.org/10.1016/j.quaint.2022.12.011

Mauritsen, T., Bader, J., Becker, T., Behrens, J., Bittner, M., Brokopf, R., et al. (2019). Developments in the MPI-M Earth system model version 1.2 (MPI-ESM1.2) and its response to increasing $CO_2$. *Journal of Advances in Modeling Earth Systems*, *11*(4), 998–1038. https://doi.org/10.1029/2018MS001400

Merz, N., Raible, C. C., & Woollings, T. (2015). North Atlantic eddy-driven jet in interglacial and glacial winter climates. *Journal of Climate*, *28*(10), 3977–3997. https://doi.org/10.1175/JCLI-D-14-00525.1

Mix, A. C., Bard, E., & Schneider, R. (2001). Environmental processes of the ice age: Land, oceans, glaciers (EPILOG). *Quaternary Science Reviews*, *20*(4), 627–657. https://doi.org/10.1016/S0277-3791(00)00145-1

Molanejad, M., Soltani, M., Ranjbar Saadat Abadi, A., Babu, C. A., Sohrabi, M., & Martin, M. V. (2015). Climatology of cyclones and their tracking over southern coasts of Caspian Sea. *International Journal of Environmental Research*, *9*(1), 117–132. https://doi.org/10.1038/s43247-021-00129-3

Molavi-Arabshahi, M., & Arpe, K. (2022). Interactions between the Caspian Sea size (level) and atmospheric circulation. *International Journal of Climatology*, *42*(16), 9626–9640. https://doi.org/10.1002/joc.7852

Molavi-Arabshahi, M., Arpe, K., & Leroy, S. A. G. (2016). Precipitation and temperature of the southwest Caspian Sea region during the last 55 years: Their trends and teleconnections with large-scale atmospheric phenomena. *International Journal of Climatology*, *36*(5), 2156–2172. https://doi.org/10.1002/joc.4483

Monnin, E., Indermühle, A., Dällenbach, A., Flückiger, J., Stauffer, B., Stocker, T. F., et al. (2001). Atmospheric $CO_2$ concentrations over the last glacial termination. *Science*, *291*(5501), 112–114. https://doi.org/10.1126/science.291.5501.112

Nandini-Weiss, S. D., Prange, M., Arpe, K., Merkel, U., & Schulz, M. (2020). Past and future impact of the winter north Atlantic oscillation in the Caspian Sea catchment area. *International Journal of Climatology*, *40*(5), 2717–2731. https://doi.org/10.1002/joc.6362

NOAA. (2022). ETOPO 2022 15 arc-second global relief model [Dataset]. *NOAA National Centers for Environmental Information*. https://doi.org/10.25921/fd45-gt74

Oster, J., Ibarra, D., Winnick, M., & Maher, K. (2015). Steering of westerly storms over western north America at the Last Glacial Maximum. *Nature Geoscience*, *8*(3), 201–215. https://doi.org/10.1038/ngeo2365

Pausata, F. S. R., Li, C., Wettstein, J., Kageyama, M., & Nisancioglu, K. (2011). The key role of topography in altering north Atlantic atmospheric circulation during the last glacial period. *Climate of the Past*, *7*(4), 1089–1101. https://doi.org/10.5194/cp-7-1089-2011

Peng, S., Li, Y., Zhang, Z., Gao, M., Chen, X., Duan, J., & Xue, Y. (2024). Simultaneous seasonal dry/wet signals in eastern and central Asia since the Last Glacial Maximum. *Climate of the Past*, *20*(11), 2415–2429. https://doi.org/10.5194/cp-20-2415-2024

Pfahl, S., O'Gorman, P. A., & Singh, M. S. (2015). Extratropical cyclones in idealized simulations of changed climates. *Journal of Climate*, *28*(23), 9373–9392. https://doi.org/10.1175/JCLI-D-14-00816.1

Pickarski, N., Kwiecien, O., Langgut, D., & Litt, T. (2015). Abrupt climate and vegetation variability of eastern Anatolia during the last glacial. *Climate of the Past*, *11*(11), 1491–1505. https://doi.org/10.5194/cp-11-1491-2015

Pinto, J. G., & Ludwig, P. (2020). Extratropical cyclones over the north Atlantic and western Europe during the Last Glacial Maximum and implications for proxy interpretation. *Climate of the Past*, *16*(2), 611–626. https://doi.org/10.5194/cp-16-611-2020

Prentice, I. C., & Harrison, S. P. (2009). Ecosystem effects of $CO_2$ concentration: Evidence from past climates. *Climate of the Past*, *5*(3), 297–307. https://doi.org/10.5194/cp-5-297-2009

Raible, C. C., Pinto, J. G., Ludwig, P., & Messmer, M. (2021). A review of past changes in extratropical cyclones in the northern hemisphere and what can be learned for the future. *WIREs Climate Change*, *12*(1), e680. https://doi.org/10.1002/wcc.680

Reyers, M., Pinto, J. G., & Paeth, H. (2013). Statistical–dynamical downscaling of present day and future precipitation regimes in the Aksu river catchment in central Asia. *Global and Planetary Change*, *107*, 36–49. https://doi.org/10.1016/j.gloplacha.2013.04.003

Richter, C., Wolf, D., Walther, F., Meng, S., Sahakyan, L., Hovakimyan, H., et al. (2020). New insights into southern Caucasian Glacial–interglacial climate conditions inferred from quaternary gastropod fauna. *Journal of Quaternary Science*, *35*(5), 634–649. https://doi.org/10.1002/jqs.3204

Rossby, C. G., Willett, H., Holmboe, M., Namias, J., Page, L., & Allen, R. (1939). Relation between variations in the intensity of the zonal circulation of the atmosphere and the displacements of the permanent centers of action atmosphere and the displacements of the permanent centers of action. *Journal of Marine Research*, *2*(1), 38–55. https://doi.org/10.1175/2010JCLI3372.1

Rowe, P. J., Mason, J., Andrews, J., Marca, A., Thomas, L., van Calsteren, P., et al. (2012). Speleothem isotopic evidence of winter rainfall variability in northeast Turkey between 77 and 6 ka. *Quaternary Science Reviews*, *45*, 60–72. https://doi.org/10.1016/j.quascirev.2012.04.013

Schaffernicht, E. J., Ludwig, P., & Shao, Y. (2020). Linkage between dust cycle and loess of the Last Glacial Maximum in Europe. *Atmospheric Chemistry and Physics*, *20*(8), 4969–4986. https://doi.org/10.5194/acp-20-4969-2020

Serykh, I., & Kostianoy, A. (2020). The links of climate change in the Caspian Sea to the Atlantic and Pacific Oceans. *Russian Meteorology and Hydrology*, *45*(6), 430–437. https://doi.org/10.3103/S1068373920060060

Shi, X., Yang, H., Danek, C., & Lohmann, G. (2020). AWI AWI-ESM1.1LR model output prepared for CMIP6 PMIP LGM [Dataset]. *Earth System Grid Federation*. https://doi.org/10.22033/ESGF/CMIP6.9330

Shumilovskikh, L., Fleitmann, D., Nowaczyk, N., Behling, H., Marret, F., Wegwerth, A., & Arz, H. (2014). Orbital- and millennial-scale environmental changes between 64 and 20 ka bp recorded in black sea sediments. *Climate of the Past*, *10*(3), 939–954. https://doi.org/10.5194/cp-10-939-2014

Sidorenko, D., Rackow, T., Jung, T., Semmler, T., Barbi, D., Danilov, S., et al. (2015). Towards multi-resolution global climate modeling with ECHAM6–FESOM. Part I: Model formulation and mean climate. *Climate Dynamics*, *44*(3–4), 757–780. https://doi.org/10.1007/s00382-014-2290-6

Sima, A., Rousseau, D.-D., Kageyama, M., Ramstein, G., Schulz, M., Balkanski, Y., et al. (2009). Imprint of north-Atlantic abrupt climate changes on western European loess deposits as viewed in a dust emission model. *Quaternary Science Reviews*, *28*(25), 2851–2866. https://doi.org/10.1016/j.quascirev.2009.07.016

Stevens, L., Djamali, M., Andrieu-Ponel, V., & Beaulieu, J.-L. D. (2012). Hydroclimatic variations over the last two glacial/interglacial cycles at Lake Urmia, Iran. *Journal of Paleolimnology*, *47*(4), 645–660. https://doi.org/10.1007/s10933-012-9588-3

Tudryn, A., Gibert-Brunet, E., Tucholka, P., Antipov, M. P., & Leroy, S. A. (2022). Chronology of the late pleistocene Caspian Sea hydrologic changes: A review of dates and proposed climate-induced driving mechanisms. *Quaternary Science Reviews*, *293*, 107672. https://doi.org/10.1016/j.quascirev.2022.107672

Ulbrich, U., Pinto, J. G., Kupfer, H., Leckebusch, G. C., Spangehl, T., & Reyers, M. (2008). Changing Northern Hemisphere storm tracks in an ensemble of IPCC climate change simulations. *Journal of Climate*, *21*(8), 1669–1679. https://doi.org/10.1175/2007JCLI1992.1

van Ulden, A. P., & van Oldenborgh, G. J. (2006). Large-scale atmospheric circulation biases and changes in global climate model simulations and their importance for climate change in central Europe. *Atmospheric Chemistry and Physics*, *6*(4), 863–881. https://doi.org/10.5194/acp-6-863-2006

van Zeist, W., & Bottema, S. (1991). Late quaternary vegetation of the near east. In *Tübinger atlas des vorderen orients/beihefte a* (Vol. 18). Reichert.

van Zeist, W., & Wright, H. (1963). Preliminary pollen studies at Lake Zeribar, Zagros Mountains, southwestern Iran. *Science*, *140*(3562), 65–67. https://doi.org/10.1126/science.140.3562.65

Vlaminck, S., Kehl, M., Rolf, C., Franz, S. O., Lauer, T., Lehndorff, E., et al. (2018). Late pleistocene dust dynamics and pedogenesis in southern Eurasia—Detailed insights from the loess profile Toshan (NE Iran). *Quaternary Science Reviews*, *180*, 75–95. https://doi.org/10.1016/j.quascirev.2017.11.010

Wang, X., Wei, H., Khormali, F., Taheri, M., Kehl, M., Frechen, M., et al. (2017). Grain-size distribution of pleistocene loess deposits in northern Iran and its palaeoclimatic implications. *Quaternary International*, *429*, 41–51. https://doi.org/10.1016/j.quaint.2016.01.058

Wegwerth, A., Ganopolski, A., Ménot, G., Kaiser, J., Dellwig, O., Bard, E., et al. (2015). Black sea temperature response to glacial millennial-scale climate variability. *Geophysical Research Letters*, *42*(19), 8147–8154. https://doi.org/10.1002/2015GL065499

Wegwerth, A., Plessen, B., Kleinhanns, I., & Arz, H. (2021). Black sea hydroclimate and coupled hydrology was strongly controlled by high-latitude glacial climate dynamics. *Communications Earth & Environment*, *2*(63), 1–8. https://doi.org/10.1038/s43247-021-00129-3

Wieners, K.-H., Giorgetta, M., Jungclaus, J., Reick, C., Esch, M., Bittner, M., et al. (2019). MPI-M MPI-ESM1.2-LR model output prepared for CMIP6 CMIP piControl [Dataset]. *Earth System Grid Federation*. https://doi.org/10.22033/ESGF/CMIP6.6675

Wigley, T., & Farmer, G. (1982). Climate of the eastern Mediterranean and near east. In J. Bintliff & W. van Zeist (Eds.), *Palaeoclimates, palaeoenvironments and human communities in the eastern Mediterranean region in later prehistory*, *B.A.R. International Series* (Vol. 133, pp. 3–37).

WMO. (2017). *WMO guidelines on the calculation of climate normals (No. 1203)*. World Meteorological Organization. Retrieved from https://library.wmo.int/viewer/55797

Wolf, A., Baker, J., Tjallingii, R., Cai, Y., Osinzev, A., Antonosyan, M., et al. (2024). Western Caucasus regional hydroclimate controlled by cold-season temperature variability since the Last Glacial Maximum. *Communications Earth & Environment*, *5*(66), 1–10. https://doi.org/10.1038/s43247-023-01151-3

Wolf, D., Lomax, J., Sahakyan, L., Hovakimyan, H., Profe, J., Schulte, P., et al. (2022). Last glacial loess dynamics in the southern Caucasus (NE-Armenia) and the phenomenon of missing loess deposition during MIS-2. *Scientific Reports*, *12*(1), 13269. https://doi.org/10.1038/s41598-022-17021-5

Xu, H., Wang, T., Wang, H., Miao, J., Chen, J., & Chen, S. (2020). The PMIP3 simulated climate changes over arid central Asia during the mid-Holocene and Last Glacial Maximum. *Acta Geologica Sinica - English Edition*, *94*(3), 725–742. https://doi.org/10.1111/1755-6724.14542

Yanina, T., Bolikhovskaya, N., Sorokin, V., Romanyuk, B., Berdnikova, A., & Tkach, N. (2021). Paleogeography of the Atelian regression in the Caspian Sea (based on drilling data). *Quaternary International*, *590*, 73–84. https://doi.org/10.1016/j.quaint.2020.07.023

Zheng, Y., Yu, G., Wang, S., Xue, B., Zhuo, D., Zeng, X., & Liu, H. (2004). Simulation of paleoclimate over east Asia at 6 ka bp and 21 ka bp by a regional climate model. *Climate Dynamics*, *23*(5), 513–529. https://doi.org/10.1007/s00382-004-0452-7